Eindhoven University of Technology

Eindhoven University of Technology

MASTER

Axial segregation in metal halide high intensity discharge lamps

van Kemenade, M.

Award date:
2004

Link to publication

Axial Segregation in Metal Halide High Intensity Discharge Lamps

M. van Kemenade
October 2004
EPG 04-18

Eindhoven University of Technology
Supervisors:
Prof. dr. ir. G.M.W. Kroesen
Dr. ir. W.W. Stoffels

Summary

In this master thesis, a study of axial segregation in metal halide high intensity discharge lamps is presented. These mercury filled lamps are enriched with additives, which radiate very efficiently in the visible spectrum. The problem with these lamps is color separation, i.e. the upper part of the lamp radiates different colors than the lower part.
In this thesis, the additive Dysprosium is studied. The radiators, like Dysprosium, are mainly situated in the lower part of the discharge in the lamp. This is due to an effect described by Fisher and is called axial segregation. Axial segregation appears, because diffusive and convective flows compete. If diffusive and convective flows are of equal magnitude, axial segregation becomes visible. To study axial segregation, the ratio between diffusion and convection is varied.
With a specially equipped airplane, different gravitational conditions are simulated by means of a pull up or free fall motion. Inside the airplane, periods of about 20s of zero G and 2G can be simulated. In zero G, convection is canceled because gravity is the driving force for convection. For the same reason convection in 2G is faster than in the normal 1G conditions.

Absorption spectroscopy is performed to determine the absolute number density of ground state Dysprosium atoms. With this density, axial segregation is studied. The author derives, explains and uses a new data analysis technique to determine the radially resolved absolute number density of ground state Dysprosium atoms.

From the studied density, it is verified that the cold spot temperature, the convective speed and the amount of mercury in the lamp influence the amount of Dysprosium in the discharge. Furthermore, it takes many tens of seconds for the cold spot temperature to settle from startup, because it takes time for the energy balance of the lamp to settle.
From the time resolved density, it is concluded that in our lamps convection is dominant under normal and hyper gravity conditions. This is in agreement with estimations made for the convection and diffusion times.
From the zero G measurements, it was determined that the two highest pressured lamps do not end up in equilibrium, 20s after the transition from 2G. The lower pressured lamp may be on the edge of being in equilibrium. This is in agreement with diffusion times of molecules, like DyI_3 and Dy_2I_6, traveling along the axis of the lamp, which are also about 20s.

More accurate estimations of diffusion and convection times can be obtained by computer simulations, but it is concluded that Fisher's model is able to explain the effect called axial segregation.

Table of contents

Table of figures

Chapter 1 Introduction

A large percentage (about 25%) of the world's energy consumption goes to lighting. By improving the efficiency of our light sources, humanity can do with less energy. This is very important, because energy is becoming increasingly scarce and in turn more expensive. A small increase in the efficiency of lamps will therefore result in a massive saving in the world's energy consumption.

This is one of the reasons a research project called ARGES (Greek for brightener) was started by the plasma group EPG of the faculty for physics of the Eindhoven University of Technology (TU/e) and Philips Central Development Lighting (CDL) some years ago.

In this master thesis, an examination of a set of metal halide high intensity discharge lamps (MH lamps or HID lamps) is presented. These lamps are very efficient due to certain additives, which mainly radiate in the visible spectrum. The visual efficiency of the HID lamps can be up to 40%, in contrast to regular light bulbs, which transform about 5% of the input power into visible light. Unfortunately, the HID lamps are not applicable for all sorts of use. To be able to use this very efficient light source for as many applications as possible, research is needed in order to gain more insight into what is happening inside of the HID lamp.

One of the problems of the HID lamp is axial segregation. This means that the additives are not distributed evenly over the discharge in the lamp, causing the color differences displayed in Figure 7. In this thesis, the author investigates the axial segregation phenomena and wants to know if the known theory can explain the axial segregation phenomena.

Axial segregation is caused by the transport of particles in the discharge of the lamp. These transports are not understood well enough, especially the diffusive and convective transports of additives. Because convection is driven by gravity, weightlessness is simulated in order to study the diffusive processes separately and hyper gravity is simulated to study the effect of an increased convective transport.

Axial segregation is studied by measuring the absolute number density of the additive Dysprosium at certain position in the discharge.

Metal Halide High Intensity Discharge lamps

Figure 1 shows an HID lamp. The lamp consists of a burner, which is a quartz cylinder with an inner diameter of 8mm, an outer diameter of 10mm and a length of 24mm. Through the burner two electrodes are positioned on opposite sides, between which a plasma or discharge can be created. A square wave current of 80Hz at 150W 'fuels' a burning lamp. Quartz is used as burner material, because the burner must be transparent and yet withstand temperatures up to 1200K. To prevent energy losses by convection of air on the outside of the burner, for protection and for UV shielding, an outer bulb, called a Buba (BuitenBallon), is added. Between the Buba and the burner, vacuum or an inert gas is present.
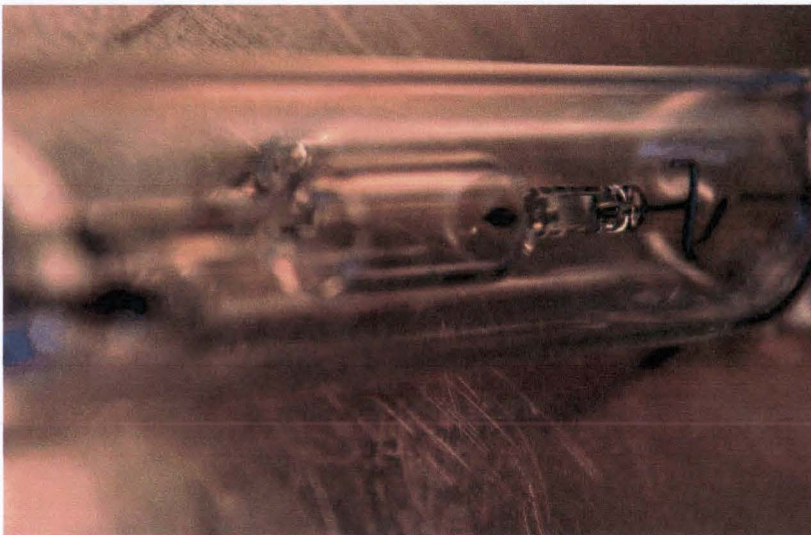
Figure 1: Photograph of an HID lamp.

The burner is filled with a starting gas, an amount of mercury (Hg) and a metal halide additive, which in our case is the salt Dysprosium tri-Iodide (DyI_3). If the lamp is turned on, a mercury plasma is formed with a pressure of 1-50bar. Due to high temperatures in the lamp, an amount of DyI_3 from the salt pool, situated underneath the bottom electrode, evaporates. The partial pressure of DyI_3 at the bottom of the lamp is typically 5-50mbar. DyI_3 enters the plasma. In the center of the plasma, high temperatures are present in which DyI_3 dissociates into Dy and I. The Dysprosium atom is a very efficient radiator and radiates at lots of wavelengths in the visible spectrum, which is the reason these lamps are very promising.

Parabolic Flight Campaign (PFC)
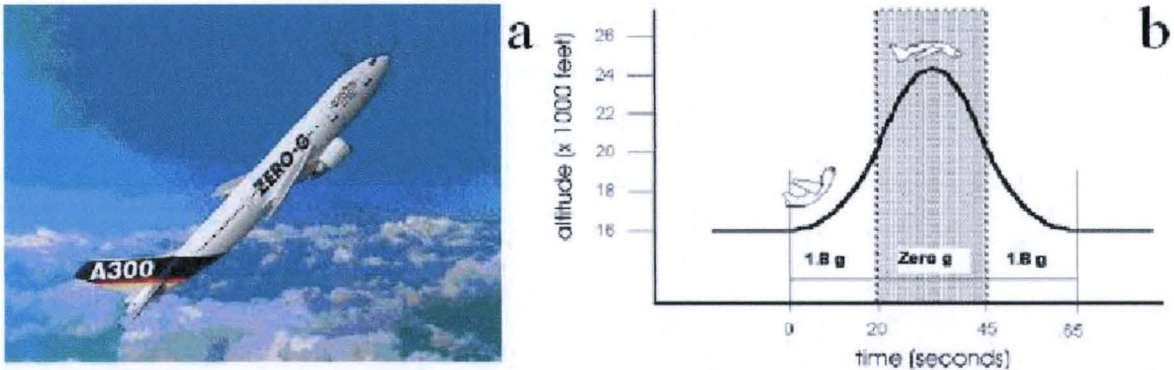
Figure 2a and b: On the left (a), the Novespace airplane specially equipped to perform PFC's. On the right (b), the parabolic sequence.

In this thesis, the amount of ground state Dysprosium atoms in experimental HID lamps will be measured during different gravitational conditions. The ratio between diffusion and convection changes with gravity, because diffusive processes do not change with different gravitational conditions, while convection is driven by gravity.

To simulate different gravitational conditions, the airplane pictured in Figure 2a is used. This plane is modified to house about 20 experiments in parabolic flight. On a day of parabolic flight, the plane performs 31 parabolic sequences of which one is pictured in Figure 2b.

When the plane is flying leveled at about 16,000feet, 1G (1 x the gravity on earth) is experienced. The plane will then pull up for about 20 seconds during which 1.8G is experienced. When the plane has an angle of about 45 degrees with the earth, a parabola is started. This means that the pilot compensates to keep all volumetric forces as close to zero as he possibly can. During this phase, which takes about 25 seconds, the path of the plane can be described by a parabola and micro gravity is experienced (~0.01G). An impression of the micro gravity phase is shown in Figure 3. At the end of the micro gravity phase, the pilot has to pull up in order to avoid crashing into the Atlantic Ocean. The second pull up phase of about 1.8G takes about 20 seconds after which 1G is re-established.

Figure 3: Photograph of the zero gravity experience. From left to right Jovita Moerel, Marc van Kemenade and Marco Haverlag are floating. The two laptops control the PFC setup. The picture is supplied by the European Space Agency ESA and is made in October 2003.

Outline of the thesis

In Chapter 2, the author will present the theory used to explain what is happening in the lamps, also the theoretical basis of the data analysis method will be given. In Chapter 3, the instrumentation will be presented and the data analysis method will be explained, shown and discussed. The results are presented in Chapter 4, in Chapter 5 conclusions are drawn and recommendations are given.

Chapter 2 Theory

In this chapter, it is stated why our lamps are NOT in Local Thermodynamic Equilibrium LTE. This will impact the other sections that follow in this chapter. The theoretical basis of the data analysis method performed on the data from the absorption spectrometer will be described. In addition, some important physical phenomena occurring in HID lamps will be described:
- Line broadening,
- Evaporation of DyI_3,
- Dissociation-recombination of DyI_3,
- Ionization of the Dysprosium atom,
- Diffusion of Dysprosium atoms and Dysprosium related molecules,
- Convection,
- Radial segregation
- And axial segregation.

Local Thermal Equilibrium (LTE)

Our lamps are not in Thermal Equilibrium TE, because line radiation leaving the plasma can be detected [7]. In TE, plank's law is valid and only radiation due to the temperature of the plasma will leave the plasma.

LTE is a departure of TE in which matter and radiation are decoupled $T_{matter} \neq T_{radiation}$ and line radiation leaves the plasma. The electron temperature, the ion temperature and the temperature of the neutrals are still equal, but gradients in both time and space keep the plasma burning. The following balances are still present in LTE:
- Boltzmann,
- Saha and
- Maxwell.

The Boltzmann balance describes the process of exitation-de-exitation of particles in a plasma. The Saha balance describes the ionization-recombination process. The Maxwell balance describes the energy distribution of the particles in the plasma. For LTE to be valid, the loss of radiation must be small compared to the exchange of energy between particles. Because the input of power is 150W and the output of light is about 50W, LTE cannot be assumed.

A more thorough investigation is required however to determine how far the plasma is from LTE. It is still possible that LTE is an accurate approximation. This is the case when the redistribution of energy states is fast enough to compensate for the loss of radiation. If departure from LTE occurs in our lamps, this will result in a higher populated ground state energy level [20].

Absorption spectroscopy

Absorption spectroscopy is chosen because it allows us to determine the absolute number density of ground state (Dysprosium) atoms in HID lamps in a direct way. Emission spectroscopy is not an option, because it is not known LTE is an acceptable approximation for the discharges. The ground state density, therefore, cannot be derived by using the Boltzmann balance. However, Boltzmann's equation must be used to determine the ground state number density using emission spectroscopy, because direct measurement of the ground state with emission spectroscopy is impossible, i.e. a ground state atom does not radiate line radiation.

To be able to use absorption spectroscopy, an equation linking the absorption of laser light to the absolute number density of ground state atoms needs to be derived.
The derivation is started with the intensity change of a beam of radiation passing through a plasma, i.e. both an absorbing and emitting medium, which can be represented by the differential equation [8]:

$$\frac{dI_v(s)}{ds} = -\kappa(v,s)I_v(s) + j_v(s) \tag{1}$$

with $I_v(s)$ the spectral intensity of the beam (in $Wm^{-2}sr^{-1}Hz^{-1}$), $j_v(s)$ the plasma emission coefficient (in $Wm^{-3}sr^{-1}Hz^{-1}$) and $\kappa(v,s)$ the absorption coefficient (in m^{-1}) for frequency v (in s^{-1}) at location s (in m). In our case, the intensity from the laser is much higher than the emission by the plasma. $j_v(s)$ will therefore be neglected.
A ground state Dysprosium atom is excited from ground state q to a higher state p if a photon with wavelength $\lambda \approx 642.19nm$ collides with the atom. Equation 2 is derived by the author in Appendix A, it states the absorption coefficient for ground state Dysprosium atoms in a discharge. This equation is valid in LTE and in non-LTE conditions with an overpopulation of the ground state.
In equation 2, A_{pq} (in s^{-1}) is the Einstein coefficient for spontaneous emission, respectively g_p and g_q are the number of states allowed to be in state p and q, $n_q(s)$ the number density of ground state Dysprosium atoms (in m^{-3}) and $\varphi_v(v,s)$ the line shape of the transition (in s^{-1}). The line shape will be explained in the next paragraph.

$$\kappa(v,s) = \frac{\lambda^2}{8\pi} \frac{g_p}{g_q} A_{pq} n_q(s) \varphi_v(v,s) \tag{2}$$

In addition, in appendix A, the absorption equation (3) is derived, which is a new equation and the basis of the analysis of the absorption spectroscopy data presented in this thesis. Note that this equation is not valid if the absorbance of the beam passing through the lamp is 100%, if the plasma emission is not negligible or if stimulated emission is not negligible.

$$\int_0^\infty \ln\left(\frac{I_{\lambda,d}(x)}{I_{\lambda,0}(x)}\right) d\lambda = -\frac{\lambda_{pq}^4 A_{pq}}{4\pi c} \frac{g_p}{g_q} \sum_{n=0}^\infty a_n f_n(x) \tag{3}$$

with $I_{\lambda,d}$ the intensity of light at wavelength λ (in m) on the detector at lateral position in the burner x (in m), $I_{\lambda,0}$ the intensity of light, if non of the photons are absorbed. c is the speed of light (in ms^{-1}), a_n is a fitting parameter and $f_n(x)$ is the nth Abel polynomial of which the first five are listed in appendix B. Note that because our measurement instrumentation is also in wavelengths, the switch was made from frequencies to wavelengths.

When the a_n's are calculated, $n_q(r)$ is known.

$$n_q(r) = \sum_{n=0}^{\infty} a_n r^n \tag{4}$$

The 100% absorption limit is not reached, if the spectral line is optically thin. However, absorption must be enough to be able to measure it. The optical thickness τ_0 of the 642.19nm line is estimated using equation 5 [23], if $\tau_0 < 1$ the line is considered optically thin.

$$\tau_0 = k_0 R_{eff} = 1.06 \cdot 10^{-5} \frac{R_{eff} f}{\pi \cdot \delta v} \cdot \frac{g_{lower} \langle n \rangle}{Q(T)} \exp\left(-\frac{E_{lower}}{k_B T}\right) \tag{5}$$

and

$$\frac{I}{I_0} \approx \exp(-\tau_0) \tag{6}$$

with [23]

$$f = A_{pq} \frac{g_p}{g_q} \cdot 1.499 * 10^4 \lambda^2 \tag{7}$$

with k_0 the absorption coefficient (in m^{-1}), R_{eff} is the effective radius (in m), which is defined as half the length of the path through the absorbing material. k_B is Boltzmann's constant (in $\text{kgs}^{-2}\text{K}^{-1}$), $<n>$ is the average number density of the absorbing atom (in m^{-3}), T is the average temperature of the plasma (in K), f is the oscillator strength and δv is the line width at FWHM (Full Width at Half Maximum) of the absorption line (in s^{-1}). E_{lower} is the energy of the lower energy state (in J). $E_{lower} = E_q = 0$, because for the line in question the lower energy state is the ground state. g_{lower} and g_q are therefore equal. $Q(T)$ is the partition function that holds the energy-weighted sum over all energy levels E_i of the neutral atomic species in LTE.

$$Q(T) = \sum_i g_i \exp\left(-\frac{E_i}{k_B T}\right) \tag{8}$$

Equations 5 and 8 can be combined, yielding

$$\tau_0 = 1.06 \cdot 10^{-5} \frac{R_{eff} f}{\pi \cdot \delta v} g_{lower} \frac{\langle n_q \rangle}{g_q} \exp\left(-\frac{E_{lower}}{k_B T}\right) \tag{9}$$

In Table 1, the estimated values used in equation 9 are presented. The absorption line is considered optically thin, because $\tau_0 < 1$. The percentage of light that will be absorbed is calculated using equation 6 and is about 45%.

Table 1: Estimated optical thickness [2] [5].

n_q in m^{-3}	R_{eff} in m	f	δv in s^{-1}	E_q in J	τ_0
10^{21}	$4*10^{-3}$	$9.98*10^{-4}$	$22*10^9$	0	0.6

Line broadening

In the paragraph above, it was mentioned that an optical transition would be scanned. This transition is of free Dysprosium atoms. Such transitions have certain line shapes, which are due to a combination of the following line broadening mechanisms [10]:

- Natural line broadening,
- Doppler line broadening,
- Resonance line broadening
- Stark line broadening,
- V.d. Waals line broadening.

Natural line broadening [10] is due to Heisenberg's uncertainty principle $\Delta E_j \cdot \Delta \tau_j \sim h$. For the line in question, the FWHM resulting from this broadening is about $3.5*10^{-8}$nm. So natural line broadening is not considered important in this thesis.

Doppler line broadening [10] is due to the well-known Doppler effect. If a particle moves from the detector, the transition will be shifted towards the red, when it moves towards the detector the transition will shift towards the blue. In a mix of very fast moving particles, in the discharge, move both towards and from the detector. The FWHM value of this broadening is about $2.6*10^{-3}$nm. This is also too small to be concerned about.

Resonance broadening is due to particles of the same kind. The discharges in question mainly consist of Hg atoms. Dysprosium particles are therefore not likely to interact with each other, because the Dysprosium particles do not interact strongly, so the Dysprosium lines will not be broadened by this mechanism.

Stark broadening is due to electrical fields. In our discharges, the electron densities are about 10^{21}m^{-3} [20], Stark broadening can therefore have a significant effect on our spectral line.

V.d.Waals broadening is due to particles of a different kind. In our plasma, the Hg atoms perturb the Dysprosium atoms. In our lamps, the number density of Hg atoms is in the order of 10^{25}m^{-3}. This means that V.d.Waals broadening can also have a significant effect on our line.

By means of a two-body-collision model, it is determined that both Stark and V.d.Waals broadening give a Lorentzian shaped line profile [10]. With emission spectroscopy, an FWHM of the total broadening of about 0.05nm is measured.

Evaporation of DyI₃

Before Dysprosium atoms enter the plasma, DyI_3 molecules must evaporate. The boiling temperature of DyI_3 is 1600K, the melting temperature is 1250K and the temperatures of the 'cold spots' of our quartz-HID lamps are about 1100K [22]. This does not mean that there is no evaporation. Above every solid, a vapor is present, especially at about 1100K.

It is concluded that there is a liquid or solid pool of DyI_3 situated at the coldest spot, also known as the 'cold spot' of the HID lamp. In equilibrium, DyI_3 vapor is formed above the cold spot and particles move in and out of the cold spot's vapor. In Table 2, some values are given for a lamp with 10mg Hg at different cold spot temperatures. A few degrees difference in cold spot temperature results in a big difference in DyI_3 vapor pressure just above the cold spot.

The temperature of the cold spot determines the maximum vapor pressure of Dysprosium in the plasma. Because the number density of Dy atoms n_{Dy} is measured, the ideal gas law (10) is used with $T = T_{eff}$=3000K [5] to estimate the average elemental number density of Dysprosium over a line of sight n_{Dy}^*.

$$p_{Dy} = n_{Dy}^* k_B T \qquad (10)$$

Table 2: The maximum elemental pressure of Dy at different cold spot temperatures, determined by the vapor pressure of DyI₃ above the solid or liquid DyI₃ [15]. The table also gives the elemental number density of Dysprosium at p_{Dy} with a plasma temperature of 3000K.

$T_{cold\,spot}$ in K	p_{Dy} in Pa	n_{Dy}^* in 10^{21} m^{-3}
1000	6.85	0.17
1010	9.52	0.23
1020	13.17	0.32
1030	18.12	0.44
1040	24.81	0.60
1050	33.80	0.82
1060	45.85	1.11
1070	61.90	1.50
1080	83.21	2.01
1090	111.37	2.69
1100	148.46	3.59
1110	197.98	4.78
1120	260.6	6.29
1130	343.3	8.29
1140	450.6	10.88
1150	589.1	14.23

It is assumed that the diffusion time between particles from the vapor to the plasma is much faster than the diffusion times of particles through the plasma.

Dissociation-recombination of DyI₃

When a DyI_3 molecule evaporates, it can travel through the HID lamp and will encounter areas with different temperatures. If temperatures are high enough, like at the center of the HID lamp, DyI_3 dissociates into DyI_2, DyI and finally into Dy and $3I$ atoms in accordance with the free energy minimization principle [2]. If temperatures are low enough, when the particles travel towards the wall of the burner, Dy and I can recombine back into DyI_3 through DyI and DyI_2, but at sufficiently low temperatures, other molecules are also possible, like Dy_2I_6.

Due to the temperature profile in the lamp [5], the particles in question, i.e. the ground state Dy atoms, will reside in the center of the plasma, where the temperature is the highest. The result is a distribution shown in Figure 4. With a radius R^*, which will be called the radius of molecular formation. Outside of this radius, almost all Dysprosium atoms have turned into molecules. Inside of this radius, the atoms freely move around, but they can also get temporarily ionized, attach themselves to other particles or get excited to a higher energy state.

In equilibrium, no net diffusive elemental flux of Dy is present and the radius of molecular formation R^* will be set. This phenomenal is called radial separation. The temperature profile along the radius of the lamp determines R^*.
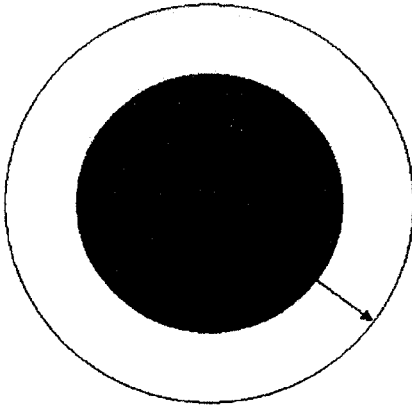
Figure 4: Schematic of a cross-section of a burning HID lamp with inner burner radius R and radius of molecular formation R^*. For $r < R^*$ the Dysprosium atom is present.

Ionization of Dy in HID lamps

Due to high temperatures in HID lamps, a certain amount of Dy atoms will be ionized [7]. In LTE, the degree of ionization obeys Saha's equation.

$$\frac{n_p}{g_p} = \frac{n_e}{g_e}\frac{n_i}{g_i}\left(\frac{h^2}{2\pi m_e k_B T_e}\right)^{3/2} \exp\left(\frac{E^{ion}_p}{k_B T_e}\right) \tag{11}$$

In Saha's equation, respectively n_p, n_i and n_e are the number density of Dy atoms in energy state p, the number density of Dy ions and the number density of electrons in the plasma. The respective constants g_p, g_i and g_e are the number of states allowed for the Dy atom in energy state p, the number of states allowed for the Dy ion and the number of states allowed for the electron. h is Plank's constant (in $m^2 kgs^{-1}$), m_e is the electronic mass (in kg) and E^{ion}_p is the ionization energy of Dy. T_e is the electron temperature in the plasma (in K).

Ionization will predominantly occur at the center of an HID lamp, because ionization strongly depends on temperature, which is highest at the center. To get an idea of the ionization degree versus radius in the lamp, Figure 5 is presented. In constructing this figure, a parabolic temperature profile is assumed with a temperature at the center ($r = 0$mm) of 5000K and a wall temperature ($r = 4$mm) of 1000K. Because Saha's equation is strongly dependant on temperature and the electron density along the radius of the lamp is not known, the electron density was considered constant along the radius of the lamp. It was assumed that $n_e = 10^{21}$m^{-3} [20]. In reality, this is of course not the case; nevertheless does Figure 5 give an impression of the ionization in the discharge.
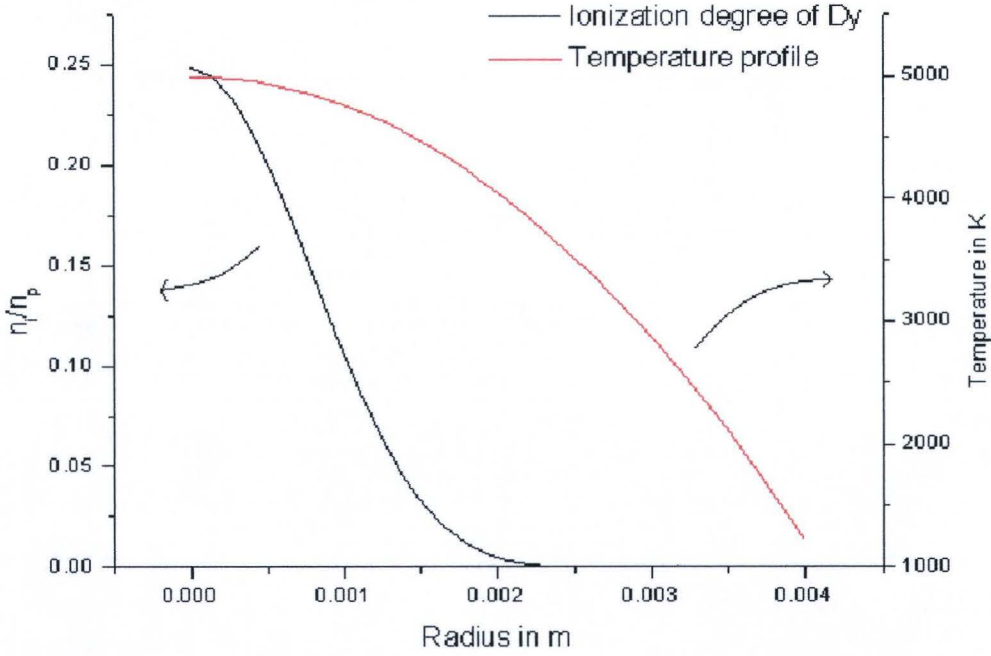
Figure 5: An impression of the ionization degree of Dysprosium in the HID lamp from a system in LTE.

Diffusion

Dy atoms typically move much faster through plasma than molecules like DyI_3 due to their larger size. Estimating the typical time of diffusion $\tau_{diffusion}$ of Dy, DyI_3 and Dy_2I_6, equations 12 to 17 [9] were used. In Table 3 and Table 7, the parameters are listed used to estimate the diffusion times along the radius of the lamp, which are presented in Table 4, and the diffusion times along the axis of the lamp, which are listed in Table 5.

$$\tau_{diffusion} = \frac{R^2}{D} \tag{12}$$

with

$$D = \frac{k_B T_{eff}}{\mu \upsilon} \tag{13}$$

and with

$$\mu = \left(\frac{1}{m_{Hg}} + \frac{1}{m_p} \right)^{-1}$$ (14)

In these equations, D is the diffusion constant (in m^2s^{-1}), T_{eff} the effective temperature in the discharge of the lamp, which is defined as the average temperature over the total volume of the discharge [5]. μ is the reduced mass (in kg), v_p the collision frequency of particle p with Hg (in s^{-1}), m_{Hg} the mass of a mercury atom and m_p the mass of the particle in question. For the collision frequency, equation 16 has to be used, which is based on solid sphere collisions. This is valid, because the particles in question (i.e. Hg, Dy, DyI$_3$ and Dy$_2$I$_6$) are neutral.

$$v_p = n_{Hg} \sigma_{Hg-p} v$$ (15)

with n_{Hg} the number density of Hg, σ_{Hg-p} the cross-section of a collision between an Hg particle and particle p (in m^2) and v the average squared velocity of the fastest particle (in ms^{-1}), i.e. Hg or particle p.

$$v = \sqrt{\frac{3k_B T_{eff}}{m}}$$ (16)

with m the mass of the particle.

$$\sigma_{Hg-p} = \pi \left(R_{Hg} + R_p \right)^2$$ (17)

with R_{Hg} the effective radius of an Hg atom and R_p the effective radius of particle p. The effective radius is defined as the radius v.d.Waals forces act.

Table 3: Parameters used to estimate typical diffusion times [16] [19].

m_{Hg} in kg	$3.3*10^{-25}$
m_{Dy} in kg	$2.7*10^{-25}$
m_I in kg	$2.1*10^{-25}$
R_{Dy} in m	$2.26*10^{-10}$
R_{DyI3} in m	$4.60*10^{-10}$
R_{Dy2I6} in m	$5.50*10^{-10}$
R_{Hg} in m	$2.09*10^{-10}$
R in m	$4*10^{-3}$
L in m	$24*10^{-3}$
T_{eff} in K	3000

Table 4: Results of estimation of diffusion times along the radius of the three measured lamps.

n_{Hg} in m^{-3}	$\tau_{Dy\ diffusion}$ in s	$\tau_{DyI3\ diffusion}$ in s	$\tau_{Dy2I6\ diffusion}$ in s
$0.97*10^{25}$	0.11	0.45	0.70
$1.45*10^{25}$	0.17	0.67	1.39
$1.93*10^{25}$	0.22	0.89	1.04

Table 5: Results of estimation of diffusion times along the axis of the three measured lamps.

n_{Hg} in m^{-3}	$\tau_{Dy\ diffusion}$ in s	$\tau_{DyI3\ diffusion}$ in s	$\tau_{Dy2I6\ diffusion}$ in s
$0.97*10^{25}$	4.0	16.1	25.1
$1.45*10^{25}$	6.0	24.1	50.0
$1.93*10^{25}$	8.1	32.1	37.5

Convection

Introducing gravity will add convection in the lamps, more gravity results in faster convective speeds. This could change the temperature profile [5] in the lamp and shift R^*. Like for diffusion, an estimate is made of the typical time of convection $\tau_{convection}$. The result of a 1G situation is presented in Table 6.

$$\tau_{convection} = \frac{L}{v_{convection}}$$ (18)

Table 6: Estimated values used to calculate the typical convection time for a discharge with $n_{Hg=1.93*10^{25}}$ m^{-3} [6].

L in m	$v_{convection}$ in ms^{-1}	$\tau_{convection}$ in s
$2.4*10^{-2}$	0.2	0.1

Radial segregation

In the section 'Diffusion', it is concluded that Dysprosium atoms diffuse faster along the radius of the lamp than Dysprosium molecules. In addition, it was concluded in the section 'Dissociation-recombination of DyI_3' that radial separation occurs due to the temperature profile along the radius of the lamp. These two facts cause the elemental number density of Dysprosium to vary along the radius of the lamp. This is called radial segregation.

During micro gravity and in equilibrium, convection is absent and the elemental Dysprosium pressure will be lower at the axis of the lamp than near the wall of the burner as pictured in Figure 6. With increasing convection, the radial segregation will gradually disappear because convection mixes the Dysprosium across the burner faster than it can segregate by means of diffusion. Note than this does not necessarily mean radial se**PA**ration disappears. At the radius of molecular formation R^*, the Dysprosium atom will still attach itself to other particles.
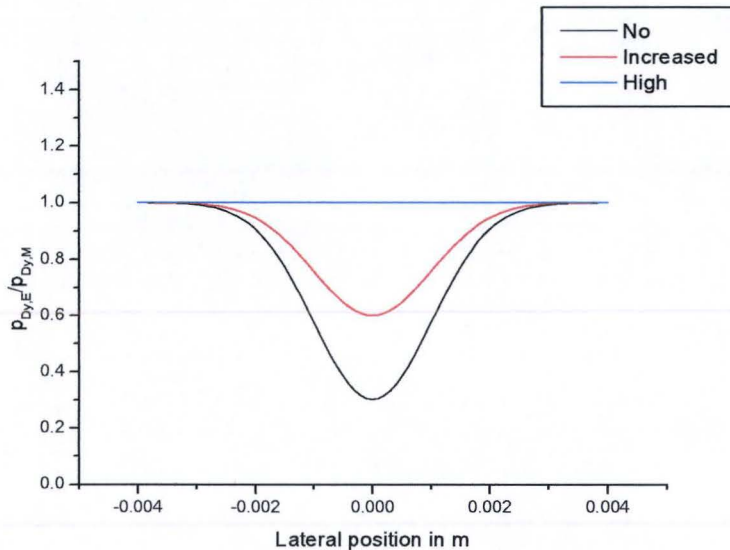
Figure 6: Sketch of radial segregation at three different convective speeds, i.e. No, Increased and High. Less radial segregation corresponds to lower convective speeds. The partial elemental pressure $p_{Dy,E}$ divided by the partial molecular pressure near the wall $p_{Dy,M}$ is pictured versus the lateral position in the burner.

Axial segregation and the Fisher curve
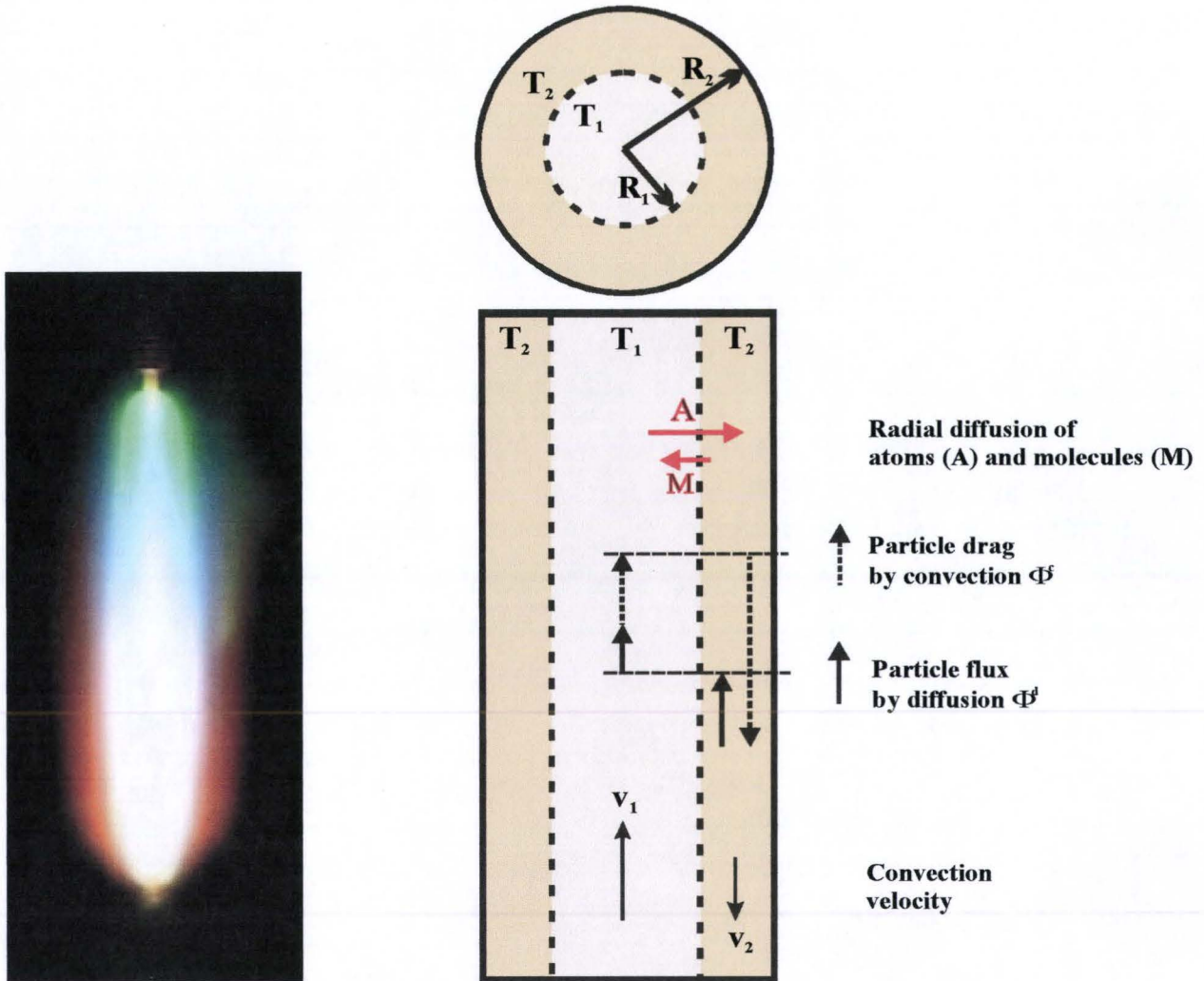
Figure 7: On the left, a photograph and on the right, a schematic of an HID lamp burning horizontally showing axial segregation. The photograph shows color separation. This is caused by the diffusive and convective fluxes shown in the schematic on the right.

As explained in the Introduction, axial segregation is present, which is pictured in Figure 7. The light emitting particles are not spread evenly within the lamp. In this section, the physical processes causing this phenomenal will be considered.

Due to a competition between diffusion and convection, schematically pictured in Figure 7, axial segregation [6] [11] is present. Fisher quantifies this competition. In Figure 8a, the Fisher curve is shown in which the axial segregation parameter λ [11] is presented, for Dy the axial segregation parameter is defined as

$$\lambda_{Dy} \equiv \frac{1}{p_{Dy}} \frac{dp_{Dy}}{dz} \tag{19}$$

with p_{Dy} the partial pressure of Dy at $r = 0$m. When gravity is low, diffusion wins the competition and the discharge has an axial segregation parameter, which is on the left hand side of the maximum of the curve

$$\lambda_{Dy} \sim p_{Hg}^2 R^2 g \ . \tag{20}$$

In our lamps $p_0 \approx p_{Hg}$, because the partial pressure of additives is much lower than the mercury pressure. When gravity is high, convection wins the competition and the axial segregation parameter of the discharge is on the right hand side of the curve

$$\lambda_{Dy} \sim \frac{1}{p_{Hg}^2 R^2 g} \ . \tag{21}$$

The axial segregation parameter can also be pictured versus gravity. This is shown in Figure 8b. At both extremes, i.e. $p_0 = 0$ and $p_0 \rightarrow \infty$ in Figure 8a or $g = 0$ and $g \rightarrow \infty$ in Figure 8b, no axial segregation is present and $\lambda = 0\text{m}^{-1}$.

At $g = 1$G and 2G our lamps are in between the two. The estimations in the section 'Diffusion' and 'Convection' show that both the time of diffusion along the radius and the convection time are of the same order of magnitude. Convection is not enough to mix the Dy through the whole of the plasma. However, it is still strong enough to compete with the radial diffusive processes, which want to distribute the Dy evenly over the radius of the plasma. Because the two processes compete, the Dy will not be distributed evenly over the plasma, as shown in Figure 7.
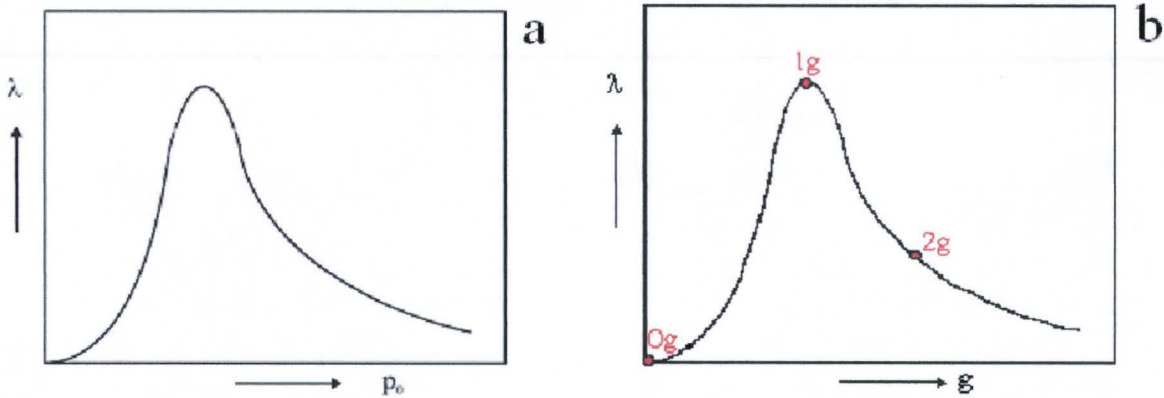
Figure 8a and b: The Fisher curve, showing the axial segregation parameter versus the pressure in the lamp p_0 on the left hand side (a) and on the right hand side (b), the axial segregation parameter versus gravity g. Note that the points indicating the 1G and 2G situation are arbitrarily chosen, they are different for differently pressured lamps.

The axial segregation parameter λ determines the number density of Dy atoms n_{Dy} versus the height in the HID lamp.

$$\frac{dn_{Dy}}{dz} = -\lambda_{Dy} n_{Dy} \tag{22}$$

$$n_{Dy}(z) = n_{Dy,0} \exp(-\lambda_{Dy} z) \tag{23}$$

In Figure 9, 3 profiles are shown. If λ is zero, profile A, a constant density along the z-axis of the lamp sets. Increasing λ will lessen the total amount of Dy in the plasma column. This can be concluded from the decrease of the surface underneath profile B and C. The number density of Dy atoms at $z = 0$m is the density just above the lower electrode. This density depends on the temperature of the cold spot and the amount of radial segregation.
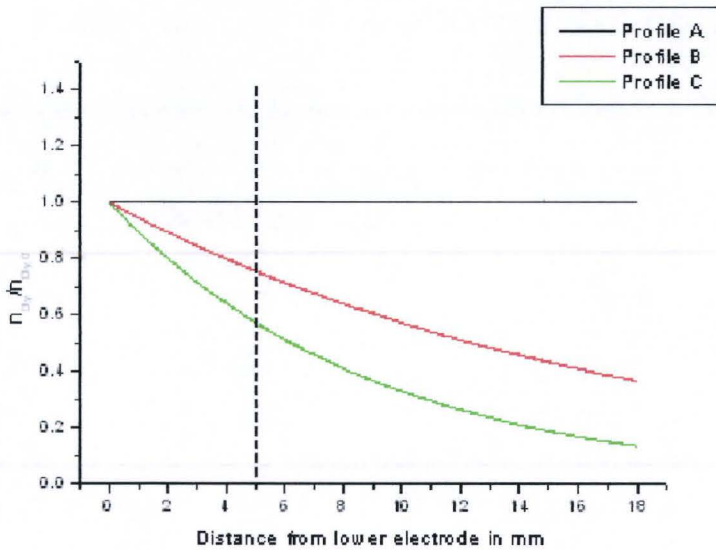
Figure 9: The number density of Dy atoms versus the height between both electrodes in the HID lamp. Different profiles show density profiles for different values of the axial segregation parameter. The axial segregation value is zero for profile A. Profile B and C have increasing axial segregation values. The place at which is measured is indicated with a dashed line at 5mm from the lower electrode.

Combining radial and axial segregation

In zero gravity, axial segregation disappears and only radial segregation is left. In this situation, the ratio between atomic and molecular Dysprosium is 0.3 as calculated by Geijtenbeek [24]. When gravity is increased the density of Dysprosium atoms increases due to less radial segregation, but the effect of axial segregation is stronger and decreases the density as shown in Figure 10.

At an unknown gravitational condition, the top of the Fisher curve is reached and at about this point the density starts increasing due to a still decreasing radial segregation in addition to a decrease in the axial segregation parameter.

Finally, when gravity is very high the discharge mixes completely. Due to high convective speeds, the atomic Dysprosium pressure becomes equal to the molecular Dysprosium pressure above the salt pool.
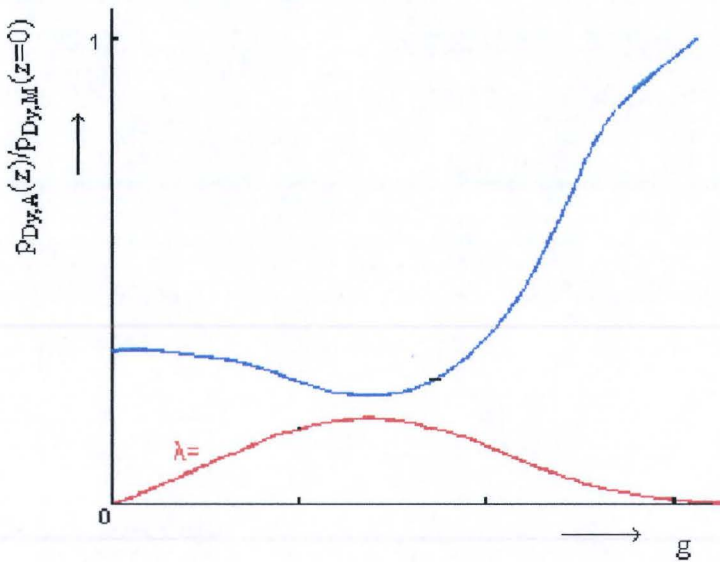
Figure 10: The blue line represents the combination of radial and axial segregation [5] on the partial atomic Dysprosium pressure at the axis of the lamp. The line starts at about 0.3. The upward trend is due to less radial segregation and the dip is caused by axial segregation. The red line is the Fisher curve described in the previous section.

Chapter 3 Instrumentation

In this chapter, the author will explain the absorption instrumentation used to measure the number density of ground state Dysprosium atoms. The lamps that will be investigated are listed in Table 7. This chapter will also explain how to calculate the number density from the data the setup collects. This section will not describe the complete experimental setup. The author points to literature for further details [1] [2] [3] [4] [5], but the laser absorption setup will be described in detail. For the list of measurements done during the PFC, the author points to Appendix E.

Table 7: Lamps measured in PFC.

Lamp number	Mercury filling in mg	n_{Hg} in 10^{25} m^{-3}
29	10	0.97
38	5	1.45
79	7.5	1.93

Global view of PFC setup

The actual experiments are preformed with an experimental setup, which is designed and build by the university workshop GTD in cooperation with the laboratory automation group of physics BLN, both of the Eindhoven University of Technology. At the military airbase of Bordeaux in June 2004, the experiment was used to gather absorption data in its third parabolic flight campaign (PFC). Previous experiments were in April 2003 and October 2003 under supervision of prof. G.M.W. Kroesen. This setup, schematically shown in Figure 11, was originally designed as a prototype for the model that went to the International Space Station ISS in 2004. The setup, therefore, had to be very light and compact.

The PFC model holds 20 experimental lamps (4) in a carousel. In Appendix D, the lamps that were used in the PFC are listed. A color camera (3), an Echelle-type emission spectrometer (6-10 and 13) and a tunable diode laser absorption spectrometer (1,2,11,12) can examine the lamps one by one.

Compared to previous PFC's, the place at which will be measured is 4mm lower along the axis of the lamps. This is 4mm from the center of the burner, 5mm above the lower electrode and 8mm from the salt pool. This is schematically shown in Figure 12.

On previous PFC's, the color camera has been used in the research of Frank van den Hout [4]. Guido Schiffelers [3] and Pim Kemps [5] have used the emission spectrometer and the absorption spectrometer is used by Danny den Akker [2].
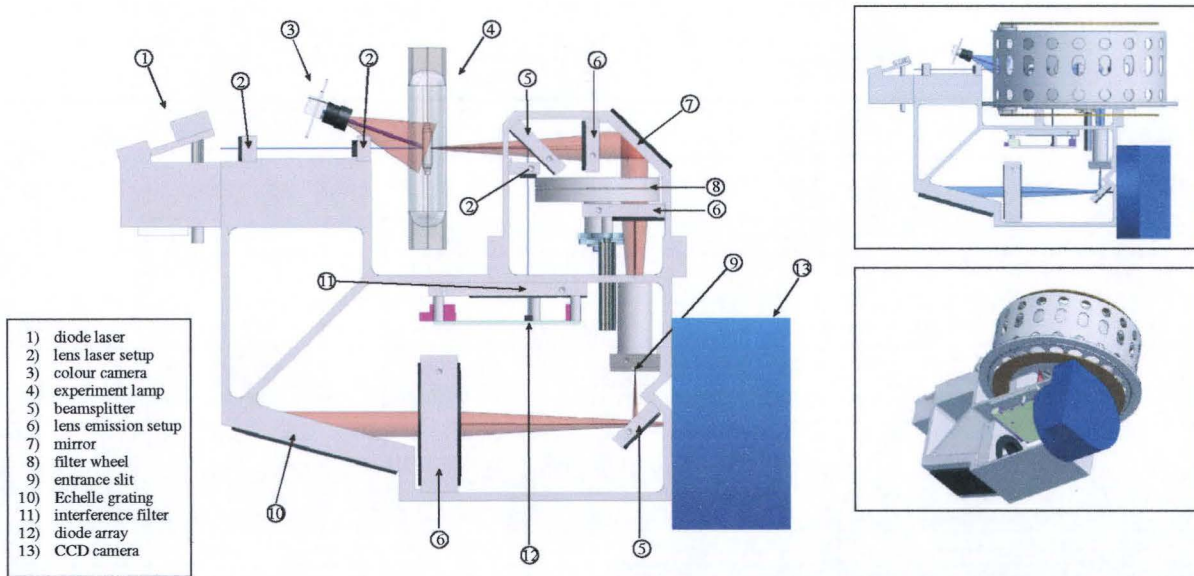
Figure 11: Schematic of the measurement instrumentation of the PFC setup designed by the GTD group of the TU/e.

1) diode laser
2) lens laser setup
3) colour camera
4) experiment lamp
5) beamsplitter
6) lens emission setup
7) mirror
8) filter wheel
9) entrance slit
10) Echelle grating
11) interference filter
12) diode array
13) CCD camera
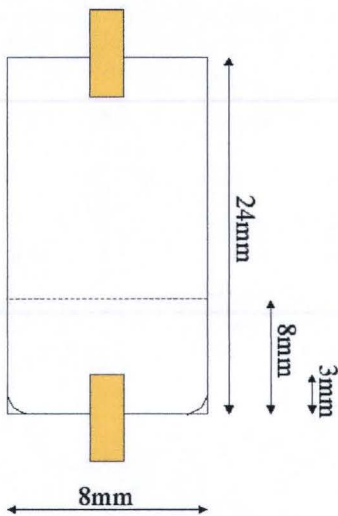
Figure 12: Schematic of the HID lamp showing the width, length, electrode height, the measurement position (dashed line) and the salt pool in the bottom corners.

The PFC setup, pictured in Figure 13, is controlled by 2 laptops also visible in the photograph in Figure 3 and a Sacher controller rack and a PhyDAS rack, which are positioned in part 1 of Figure 13 and pictured in Figure 14.

The laptop above part 2 in Figure 13 will be called laptop A. With this laptop, the carousel is rotated in order to change lamps, lamps are started, different powers up to 150W can be applied to the lamp, filters for the emission spectrometer are changed and the color camera is operated. The other laptop, which will be called laptop B, is used to control some parameters for the laser and emission setup.
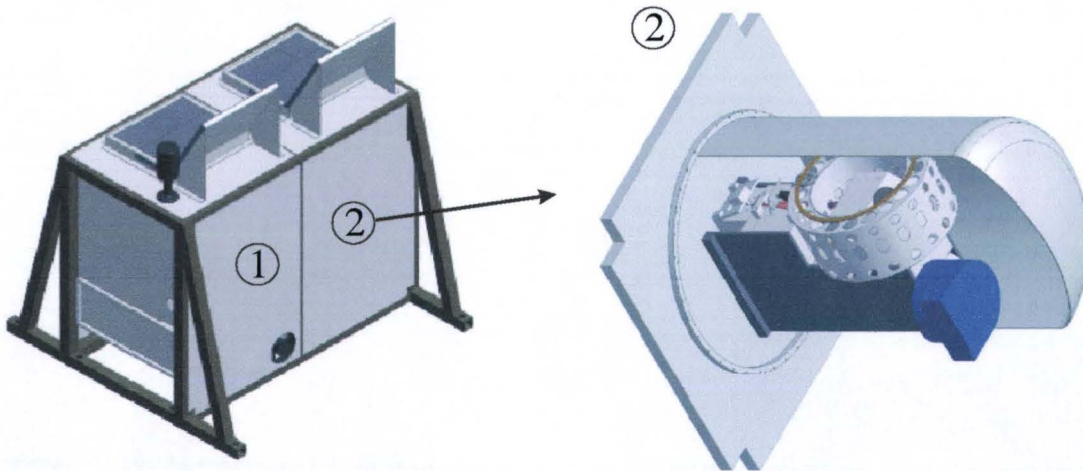
Figure 13: Drawing of the PFC setup.

Figure 14: Photograph of a side of the PFC setup at which the SACHER controller rack and the PhyDAS rack are located.

22

Laser absorption setup

The absorption setup consists of a tunable diode laser [17] that emits light at about 8mW of power with a wavelength of about 642.19nm, which is the absorption line of the ground state Dysprosium atoms in question. The laser beam passes some lenses, the HID lamp and an interference filter as pictured in Figure 15. Finally, the laser beam hits the detector, which is an array of photo diodes that counts the number of photons it collects. If there are ground state Dysprosium atoms present in the plasma, some photons will be absorbed and less photons will be collected on the detector.

cross-section

laser   lens I   lens II   lens III   diode array

burner and
outer balloon

interference
filter
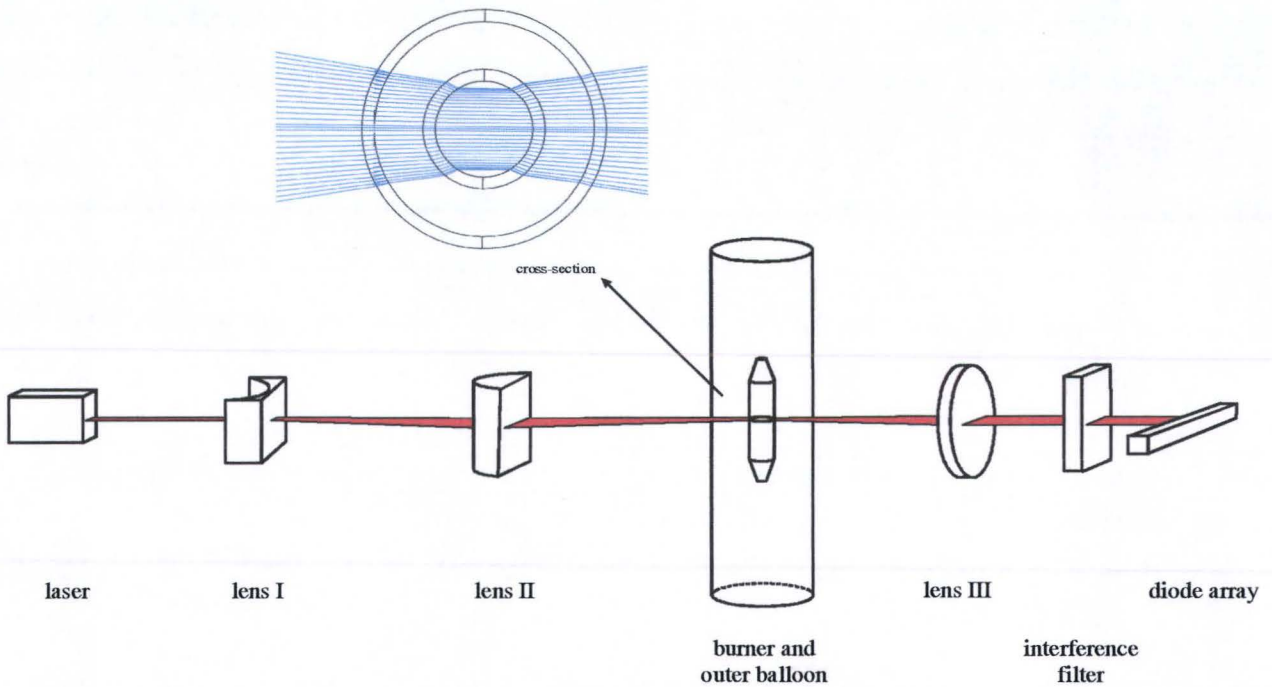
Figure 15: Schematic of the optical system of the absorption setup. With a ray trace program, the laser beam is pictured going through the burner. With the ray trace program, a one on one relationship between the ray through the burner and the detector position can be determined.

The interference filter lets light with certain wavelengths pass, as shown in Figure 16. This means that there will also be photons that are emitted by the plasma and not only from the 642.19nm line that hit the detector when the lamp is turned on. For this fact will be corrected in the data analysis.
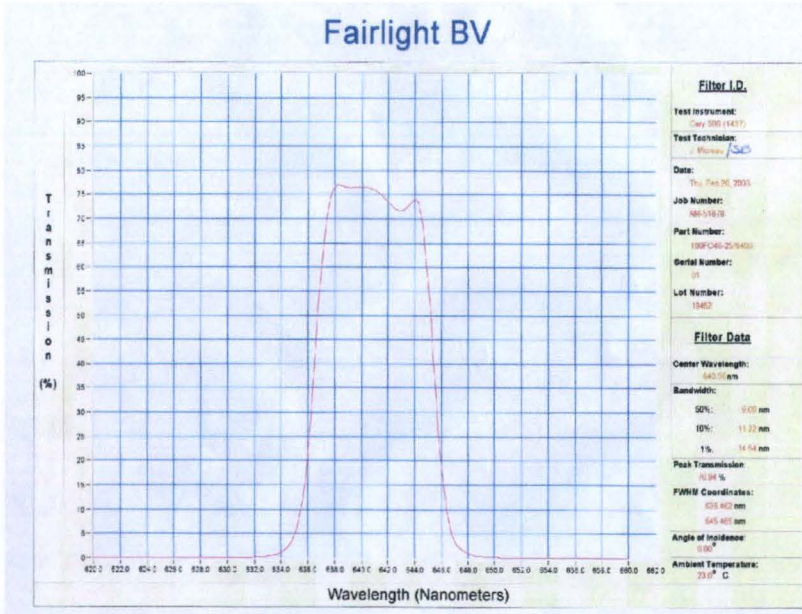
Figure 16: Transmittance of the interference filter in the PFC setup.

The detector consists of 32 evenly spaced photo diodes. However, due to the lens formation, the lateral positions in the burner of the lamp are not evenly spaced. By means of ray tracing, the dependence, shown in Figure 17, between the photo diode and lateral position x_{lat} is given. Detector number $d = 0$ is the center diode. The fifth order polynomial fit of the points is:

$$x_{lat} = 6.22 * 10^{-4} d - 5.35 * 10^{-5} d^2 + 2.69 * 10^{-6} d^3 - 8.93 * 10^{-8} d^4 + 2.16 * 10^{-9} d^5 \qquad (24)$$
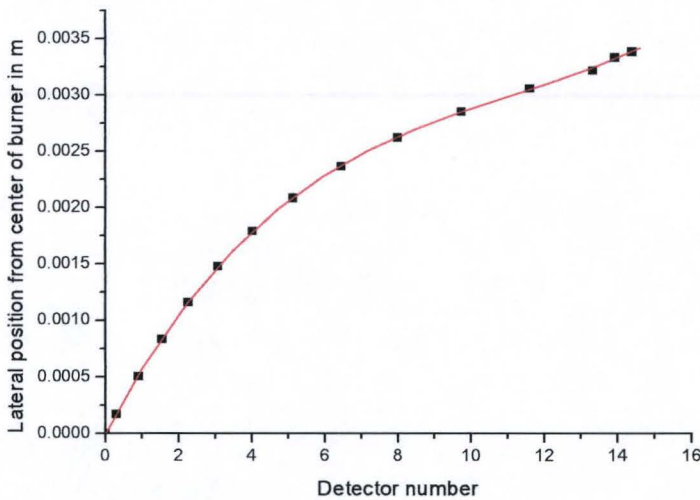
Figure 17: The lateral position from the center of the burner versus the detector number counted from the center diode. The last point at x_{lat} = 3.28mm is the maximum distance from the center measurable.

Ray tracing calculates the path of a beam of light, using optical refraction equations, not the thin lens equations. Because the laser has a certain beam width, aberrations appear. Figure 18 shows that the beam width leads to a crossing of lines, so the one on one relationship mentioned above is broken, i.e. Figure 17 becomes invalid.
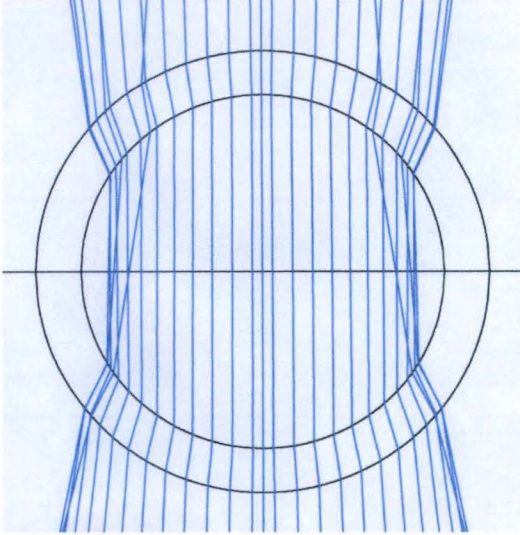
Figure 18: Schematic of rays of light, coming from above, passing the burner. The picture is made with a ray trace program. The picture shows aberrations caused by a widened laser beam.

The laser diode is an optical resonator, which has multiple modes that are amplified. The difference in frequency between the modes is given by

$$\Delta v = \frac{c}{2nl}$$
(25)

with n=3.66 the refractive index of GaAs and $l \approx 300\mu m$ the length of the optical resonator. If the laser is operated at 642nm, the spacing between modes is about 0.2nm. The width of a mode is typically in the order of 10^{-4}nm, which makes this laser capable of performing absorption spectroscopy on ~0.4nm wide lines.

To select a mode the laser is tuned with an extended/external cavity, known as a 'Littman configured wavelength selection' configuration, which is pictured in Figure 19. Note that by extending the cavity, the spacing between modes decreases to about 10^{-2}nm. The mirror guides the first order of diffraction on the grating back into the laser cavity. The photons of this beam will be multiplied, so only one mode is multiplied by a constant (gain) higher than one and the laser will be operating in single mode. The exit beam is the zeroth order of diffraction on the grating. Applying a voltage between 0 and 100V to the piezo element changes both the orientation of the mirror and the length of the cavity. This means shifting both the red and blue line in Figure 20.

The shift of both the red and blue lines, shown in Figure 20, has to be synchronized otherwise mode hops will appear. A mode hop is when the laser jumps from one cavity mode to another ($\Delta\lambda \approx 10^{-2}$nm) resulting in a change in wavelength that is not continuous.
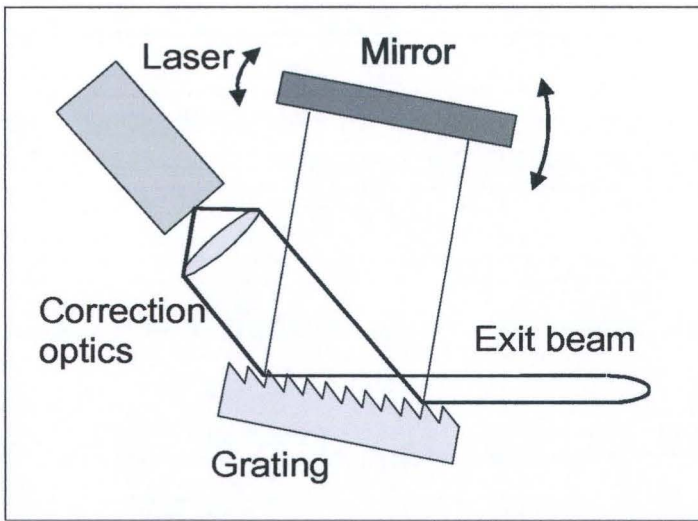
Figure 19: Schematic of the extended/external cavity tuning the laser [17]. A change in position of the mirror changes both the length of the cavity of the laser and the angle the light hits the grating.
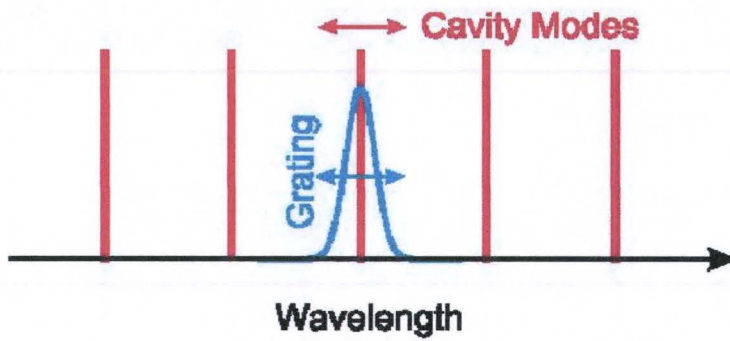
Figure 20: Possible modes in the cavity with a grating selecting one [17].

Operating the laser
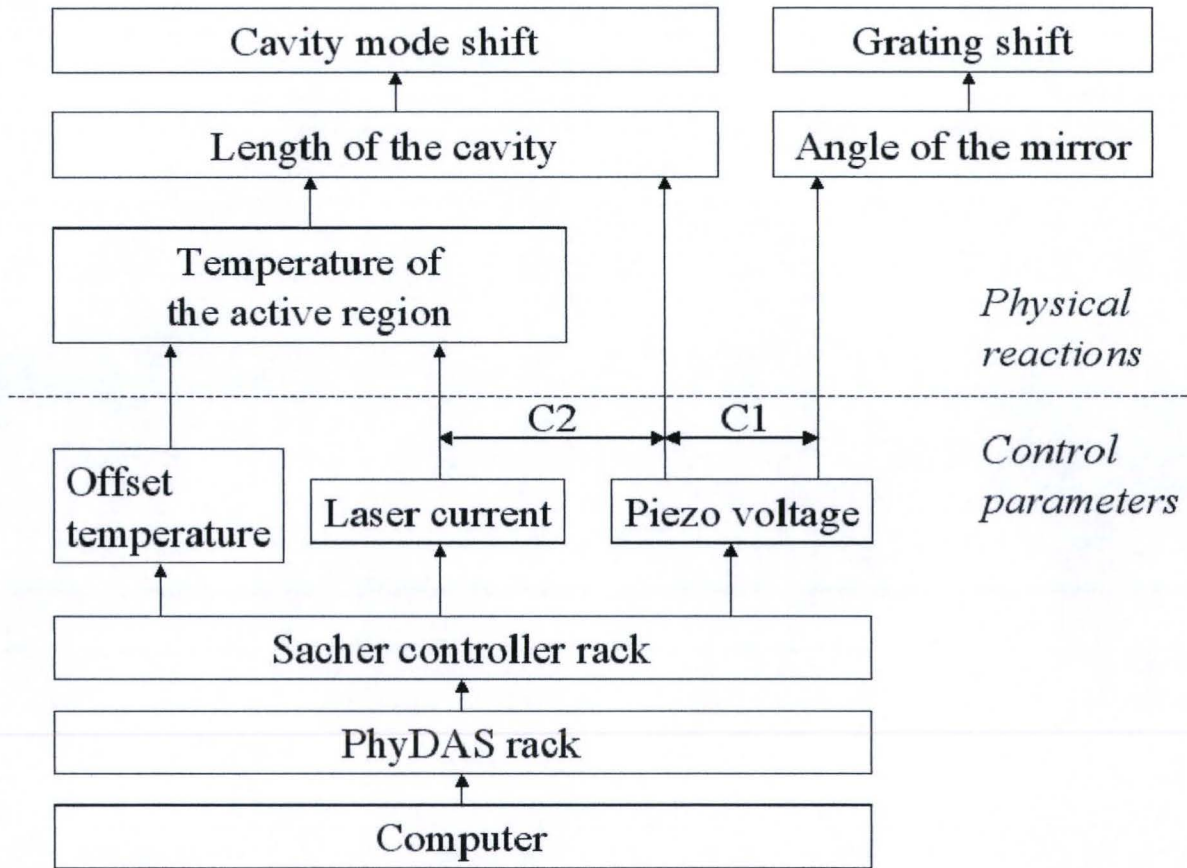
Figure 21: The laser operating system. With below the dashed line the instrument settings and above the line the results of these settings. C1 and C2 are couplings. C1 is a mechanical coupling and is always present. C2 is an electronical coupling, which can be turned on and off. The goal is to synchronize the cavity mode shift and the grating shift. This is done by three input parameters that control the cavity shift and one input parameter controlling the grating shift.

In Figure 21, the scheme that explains the operating system of the laser is shown. The goal of the operating system is to have a synchronized shift of the cavity mode and the grating. With a synchronized shift, $I_{\lambda,d}$ and $I_{\lambda,0}$ from the absorption equation (3) are measured on the 642.19nm absorption line.

The cavity mode shifts, if the length of the cavity changes. The three parameters controlling the cavity length, i.e. the offset temperature, the laser current and the piezo voltage, have to vary such that they keep up with the grating shift, controlled by only one parameter, i.e. the piezo voltage.

Through the computer, the PhyDAS rack and the Sacher control rack, the three parameters of the laser system, i.e. the temperature of the active region of the laser, current through the laser diode and piezo voltage, can be adjusted.

The laser temperature must first be set to a certain operating temperature, which is done with the Sacher control rack. This operating temperature is controlled by a Peltier element. In our experiments, the operating temperature is set at 30°C.

Next, the 642.19nm absorption line must be found by setting the piezo voltage. Changing the piezo voltage on the Sacher controller rack changes both the length of the cavity and the angle of the mirror, because they are mechanically coupled, as shown in Figure 19 and C1 in Figure 21.

To extend the range of the mode hop free zone, the current is electronically coupled to the piezo voltage, C2 in Figure 21. The current heats the active region of the laser somewhat so the length of the cavity increases and a better synchronization between the shifts is accomplished.

The drawback is that this electronic coupling imposes a limit to the maximum scanning range, called the span, this is due to a minimum and maximum current at which the laser operates [18]. The minimum current of about 29mA is the threshold current at with the laser starts lasering. There have to be enough exited electrons for the gain to be larger than one. The laser's maximum current is 80mA, because the semiconductor would degrade very fast if operated at higher currents.

Our system limits us, due to the coupling of current and voltage to a 40V scan, just enough to scan the mean part of the 642.19nm absorption line of Dysprosium. The result of a change from 0 to 100V in the piezo voltage is a change in wavelength of the exit beam of up to 0.5nm.

In Figure 22, the signal on the detector when the lamp is off is shown. The shape of the signal is triangular, because of the current coupling. If the current is raised the power of the laser also rises, resulting in more signal on the detector. When the current decreases, the power of the laser also decreases. Keep in mind that the line shape is therefore scanned twice.

Above 'Measurement channel' in Figure 22, the piezo voltage and the piezo span are set. It is best to set the piezo voltage to zero, because it is easier to control the parameter with one instrument, i.e. the pot meter on the Sacher control rack. The piezo span is set to 4.000V and with the amplifier in the Sacher control rack this results in a triangular signal on the piezo with a span of 40V.

The Sacher control rack controls the offset voltage applied to the piezo. This voltage is the offset above which the 40V span is put. The piezo voltage can therefore be set to a maximum of 80V because the piezo cannot handle voltages above 120V. The rack also controls the current for the laser diode.

Improvements

Compared to previous experiments, the author has made an important but simple improvement. A shutter has been placed between the first and second lens of Figure 15 in order to block the beam, when performing an emission measurement. In previous experiments, the laser was turned on and off in order to perform emission measurements. The change was made because the laser system will slow start until a thermal equilibrium is established in the laser diode, which can take some tens of seconds. During this time, it is not possible to do absorption measurements.
A software update can be seen in Figure 22, a screenshot of laptop B. In the bottom left graph the four lines represent measurements on different photo diodes. In previous PFC's, only one line could be monitored. It was considered best to monitor more lines in the graph. The diodes can be selected with the four numbers in the boxes underneath 'Measurement channel'.
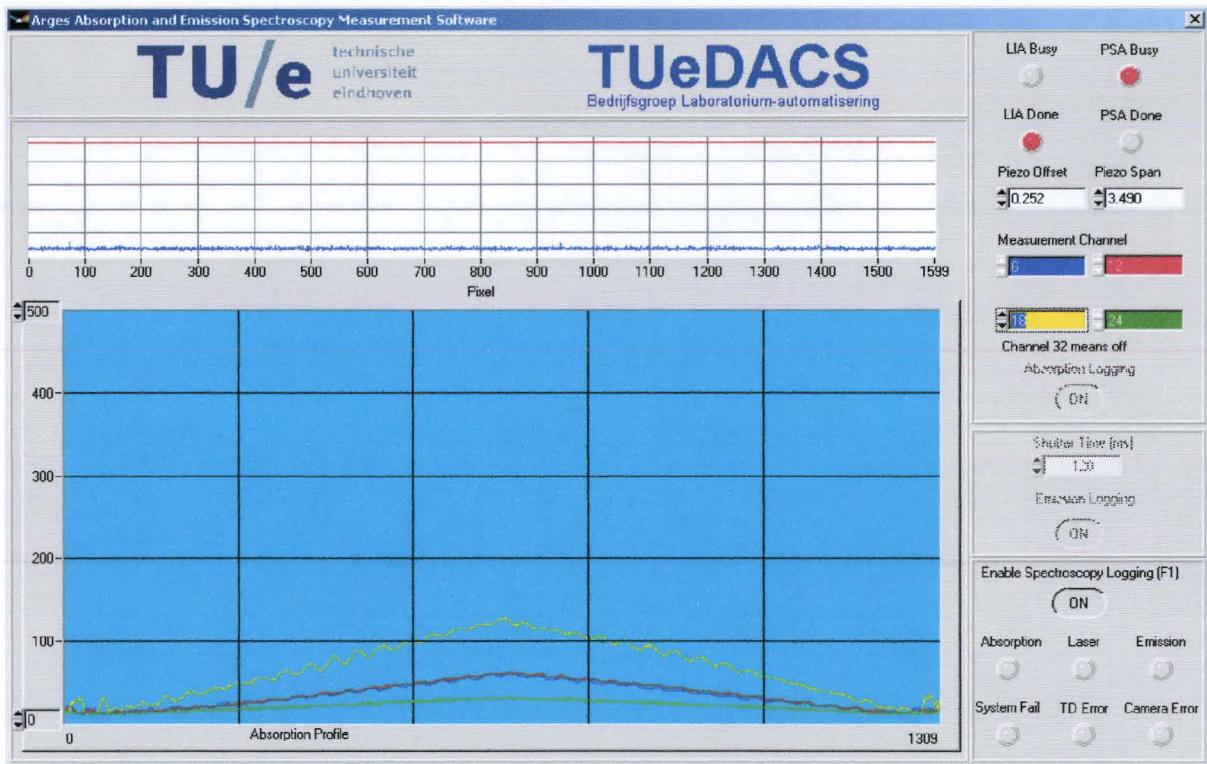
Figure 22: Screenshot of laptop B controlling the emission and absorption measurements.

Data handling

In order to calculate the density profile, the absorption equation (3) is needed. The inputs of the equation are multiple scans at different lateral positions of the line shape of the optical transition with $\lambda = 642.19$nm and background measurements at these positions.
In this section, the author will take the reader through the steps of data processing and in Appendix B the ORIGIN scripts, which do the actual work are listed.

Step 1: The measurements

In Figure 23a, both a measurement of the optical transition and a background measurement of one lateral position are displayed. Because the voltage varies in time, the time axis could have been replaced by a wavelength axis. Due to the in time triangular shaped voltage applied to the piezo of the laser, the wavelength of the laser will first increase followed by a decrease of the wavelength. The transition point is at about $t = 0$a.u., the line shape is therefore scanned twice, in mirror image of each other. The increase and decrease in signal is, as mentioned above, due to current coupling. An increase in piezo voltage results in an increase in the current ran through the laser, which increases the power of the laser.

Step 2: Synchronization

A problem is that the transition from increasing to decreasing wavelengths is not exactly at $t = 0$a.u., this means that the wavelengths of both lines at for example $t = 100$a.u. in Figure 23a are not equal. The lines will, therefore, be shifted so the maximum of both lines in Figure 23a are at $t = 0$a.u. However, due to the high noise level of the lines, an FFT filter must first be used. This is a low pass filter, to get rid of the noise. The result of the FFT filter is pictured in Figure 23b. The shift of Figure 23a is pictured in Figure 23c.

Step 3: Clearing noise

The raw signal must first be centered before the final FFT filtering, because there is a continuous triangular signal on the piezo and parts of a previous or next triangle would otherwise be included, as shown by the arrow in Figure 23b.
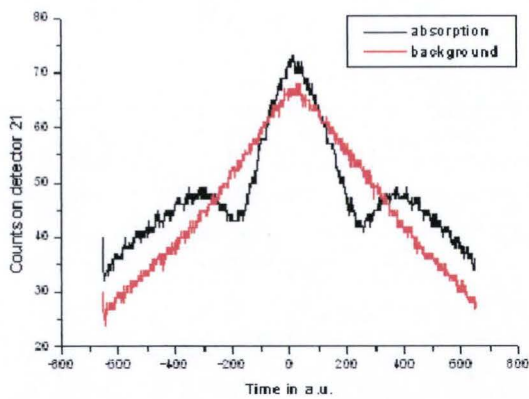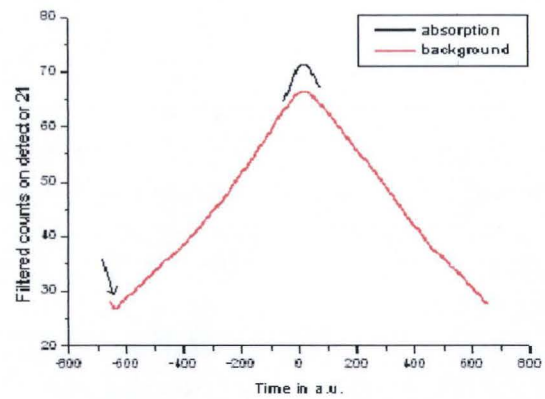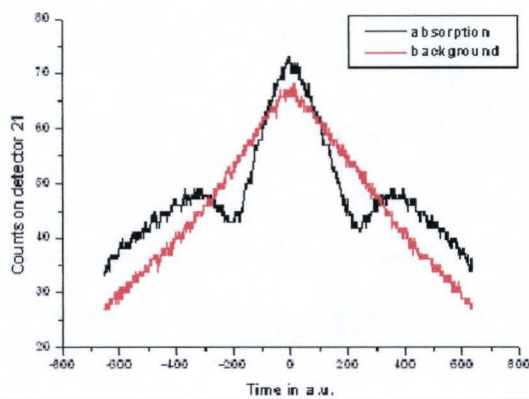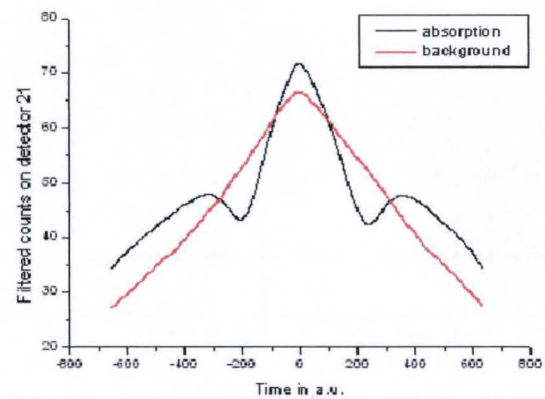
Figure 23a to d: Part one of the conversion of measurement data into number densities in lamps.

Step 4: Correcting for emission

A detector continuously receives light emitted from the lamp, a constant must, therefore, be subtracted from the FFT filtered absorption measurement. The emitted light is not only from the 642.19nm line, the interference filter in the setup has a width of about 4nm, as mentioned in Chapter 3 'Laser absorption setup', so the assumption made in Chapter 2 'Absorption spectroscopy', i.e. that the emission the spectral line in question is negligible, is still valid. The result of this correction is displayed in Figure 24a.

Step 5: Line shape determination

By dividing the two lines in Figure 24a, the absorption line shapes, pictured in Figure 24b, are calculated. In the Figure 23a to d and Figure 24a and b, the negative times are increasing wavelengths, the positive times are decreasing wavelengths, as explained in Step 1.
The line shape in Figure 24c is calculated by averaging the mirror image of the line shape on the left hand side with the line shape on the right hand side. This line shape is the term between brackets on the left hand side of the absorption equation (3).

Step 6: The left hand side of the absorption equation

The absorption equation (3) states that the natural logarithm of the line shape of Figure 24c has to be calculated, which results in Figure 24d. The absorption equation (3) also states that this result must be integrated over the wavelengths.
The parameter A of the Lorentz function (26) gives the area underneath Figure 24d.

$$y = \frac{2A}{\pi} \frac{w}{4(x - x_c)^2 + w^2} \tag{26}$$

A Lorentz is therefore fitted through the line in Figure 24d. This is done because complete scans of the line shape were not obtainable and by fitting the Lorentz; the remaining parts (the wings) of the line shape are included.
Note that the Lorentzian is chosen because it gives a good fit, Figure 24c and d are not Lorentzian in nature, as explained in Chapter 2 'Line broadening'. The line shape at a particular radius is probably a Lorentzian, but this cannot be measured. What is measured is the absorption line shape at the end of a line of sight, which a different thing.
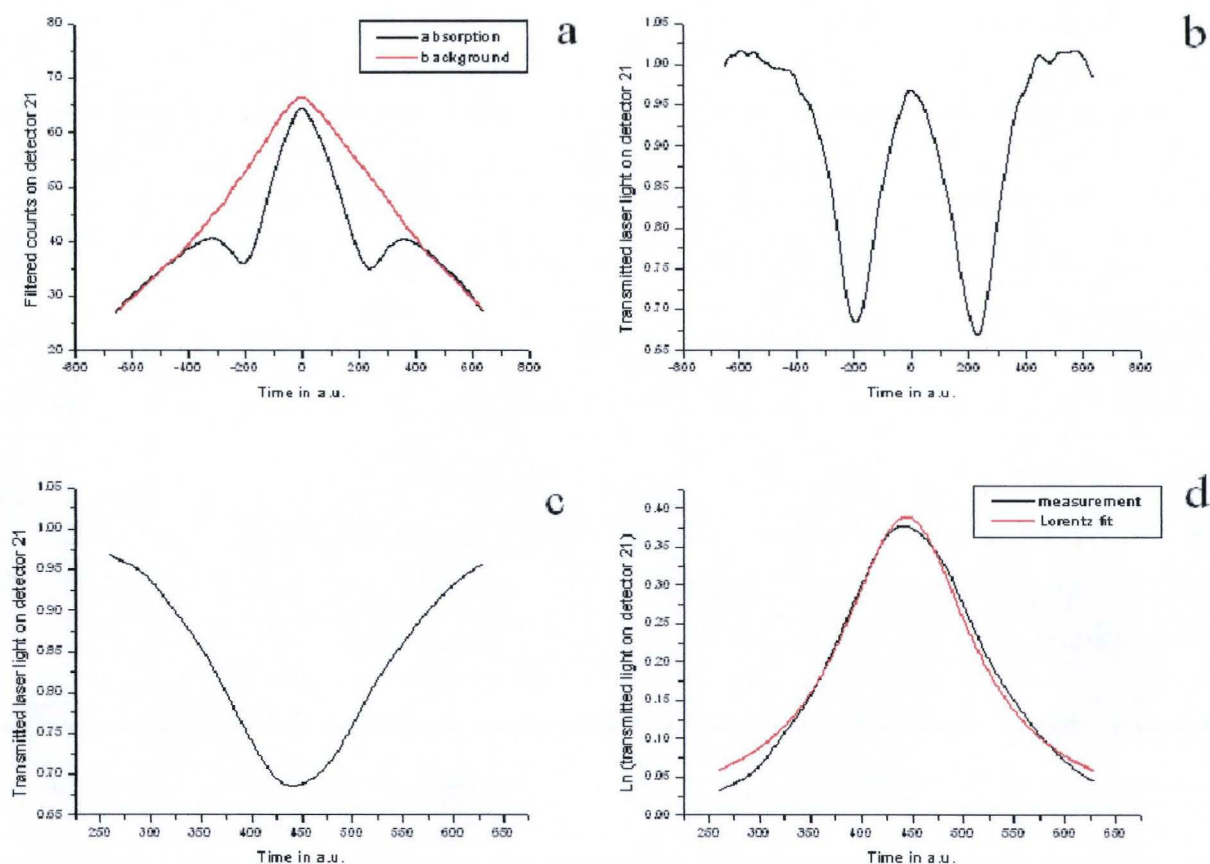
Figure 24a to d: Part two of the conversion of measurement data into number densities in lamps.

Steps 1 to 6 describe the gathering of only one point in Figure 25. This process has to be repeated for another 31 lateral positions in order to obtain the information needed in the term on the left hand side of the absorption equation (3).

Step 7: Clearing faulty points

In Figure 25, some points are deleted, because due to the aberrations discussed in Chapter 3 'Laser absorption setup', these points are from other lateral positions and shall therefore be disregarded.

Step 8: The right hand side of the absorption equation

The radially resolved absolute number density of ground state Dy atoms in the burner of the HID lamp can be determined by fitting the remaining points with Abel polynomials ($f_n(x)$'s), convert the time axis of Figure 24d into wavelengths and multiply by the constants on the right hand side of the absorption equation (3).
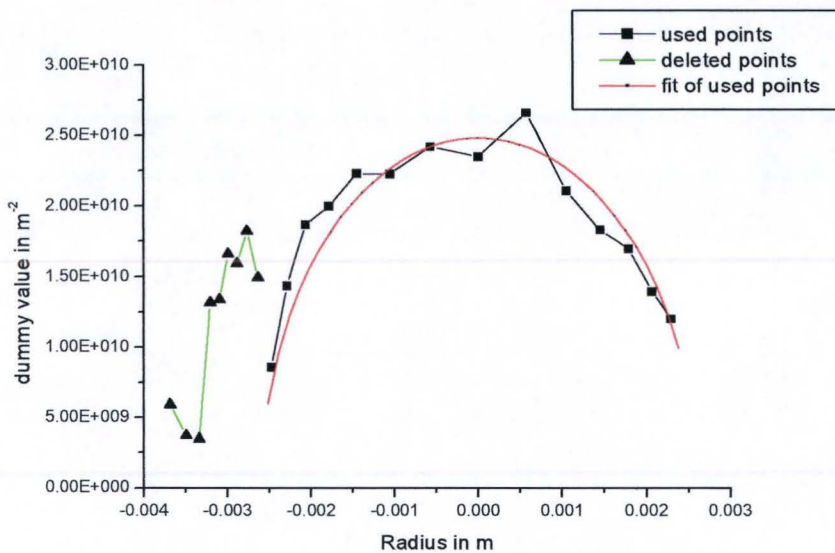
Figure 25: Part three of the conversion of measurement data into number densities in lamps.

Comparing fitting procedures

In Figure 26, the number density versus the radius in the burner of the 5mg Hg filled lamp is shown. The figure holds three lines representing the three different fitting procedures. The simplest fitting procedure was also used in the section above, it discards all a_n's from the absorption equation (3) except for a_0 and uses R^* instead of R. With this fitting procedure, the average number density within the radius of molecular formation R^* is calculated. This means the absorption equation (3) becomes:

$$\int_0^\infty \ln\left(\frac{I_{\lambda,d}(x)}{I_{\lambda,0}(x)}\right) d\lambda = -\frac{\lambda_{pq}^4 A_{pq}}{4\pi c}\frac{g_p}{g_q} a_0 f_0(x) \qquad\qquad \text{with} \quad -R^* \le x \le R^* \quad (27)$$

and

$$n_{Dy} = a_0 \qquad\qquad \text{with} \quad 0 \le r \le R^* \quad (28)$$

The a0a2a3 fit discards all but a_0, a_2, a_3 and uses R^*, so a density profile versus the radius r is calculated. The absorption equation (3) becomes:

$$\int_0^\infty \ln\left(\frac{I_{\lambda,d}(x)}{I_{\lambda,0}(x)}\right) d\lambda = -\frac{\lambda_{pq}^4 A_{pq}}{4\pi c}\frac{g_p}{g_q} \left(a_0 f_0(x) + a_2 f_2(x) + a_3 f_3(x)\right) \qquad \text{with} \quad -R^* \le x \le R^* \quad (29)$$

and

$$n_{Dy} = a_0 + a_2 r^2 + a_3 r^3 \qquad\qquad \text{with} \quad 0 \le r \le R^* \quad (30)$$

In the a0a2a3 fit with a boundary condition BC, the same parameters as in the a0a2a3 fit are calculated, but the condition that at R^* the density should be zero is included, i.e.

$$a_0 + a_2 \left(R^*\right)^2 + a_3 \left(R^*\right)^3 = 0 \qquad\qquad (31)$$

Number density of ground state Dy atoms in m^{-3}

2.50E+021
2.00E+021
1.50E+021
1.00E+021
5.00E+020
0.00E+000

0.0000 0.0005 0.0010 0.0015 0.0020 0.0025 0.0030 0.0035 0.0040

Radius in m

Legend:
— a0 fit
— a0a2a3 fit
— a0a2a3 fit with BC
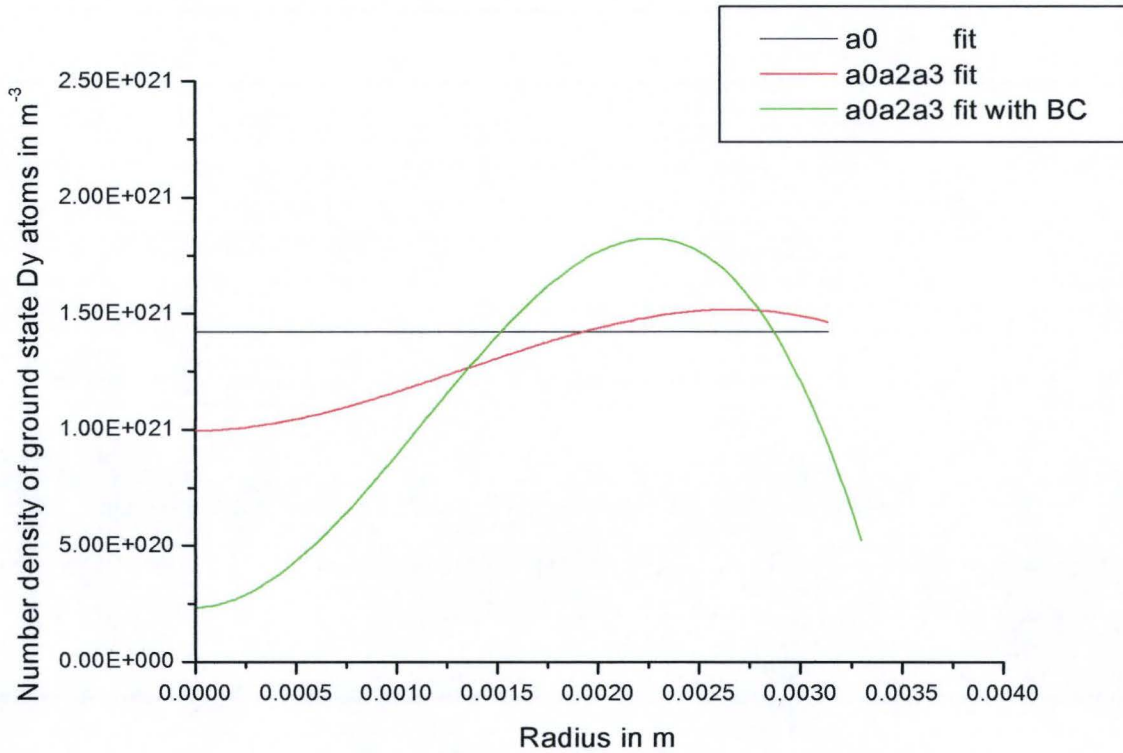
Figure 26: The number density of ground state Dy atoms versus the radius of the 5mg Hg filled lamp. The three lines represent three different fitting procedures. A different radius of molecular formation for each of the lines is determined, for the a0 fit $R^* = 3.14$mm, for the a0a2a3 fit is $R^* = 3.14$mm and for the a0a2a3 fit with BC $R^* = 3.3$mm.

Figure 26 shows a dramatic change in the density plot, which is due to the application of the boundary condition. The boundary condition gets rid of the infinitely steep slope at R^*. The dramatic change is due to the basis of eigenfunctions, which is too small. The rim at R^* is too steep for a third order polynomial to handle and the fit becomes unreliable. This is an important discovery, because it was believed to be the case that the density of Dysprosium atoms would more gradually decline.

From the above we conclude that the a0a2a3 fit is the most realistic one, it is an improvement of the a0 fit. However, because only few data points are available (Figure 25), the stability of the a0 fit is considered better than the a0a2a3 fit. It is therefore considered best to use the a0 fit in comparing different gravitational conditions, which will be done in the next chapter. In the future, if more data points in the lateral direction are available, radially resolved density profiles could be determined with the absorption equation (3).

We can still conclude from the density profile resulting from the a0a2a3 fit that at the center, the density is lower than just before R^*, which is due to radial segregation, ionization and excitation of the Dysprosium atom. In the center of the discharge, temperatures are higher, so more atoms will be ionized and excited.

Chapter 4 Results

Startup phase of a lamp

Figure 27: The startup phase of the 7.5mg Hg HID lamp in which two parabolas are present. To increase the clarity of the graph, the error bars are absent. The average error is about 5 percent.

In Figure 27, the average number density within the radius of molecular formation R^* of the startup of the 5mg Hg filled HID lamp is displayed. Unfortunately, there is a parabola during the time of startup. However, by comparing the first parabola with the second, starting at about $t = 190s$, a rise time in the order of tens of seconds is still apparent.

When starting an HID lamp, it takes some time for the additive to end up in the plasma. The long diffusion time along the axis of the lamp of DyI_3 (Table 5) is not the cause of the slow rise, because convection disperses the DyI_3, which is a much faster process ($\tau_{convection} \approx 0.1s$). From Figure 27, we conclude that it takes time for the energy balance of the burner to settle and a time constant can be linked to this process, which is at least in the order of tens of seconds.

Number density versus time

Before going into details about radial and axial segregation, the absolute number density of Dysprosium will be linked to the cold spot temperature. This is done to validate the absorption equation (3).

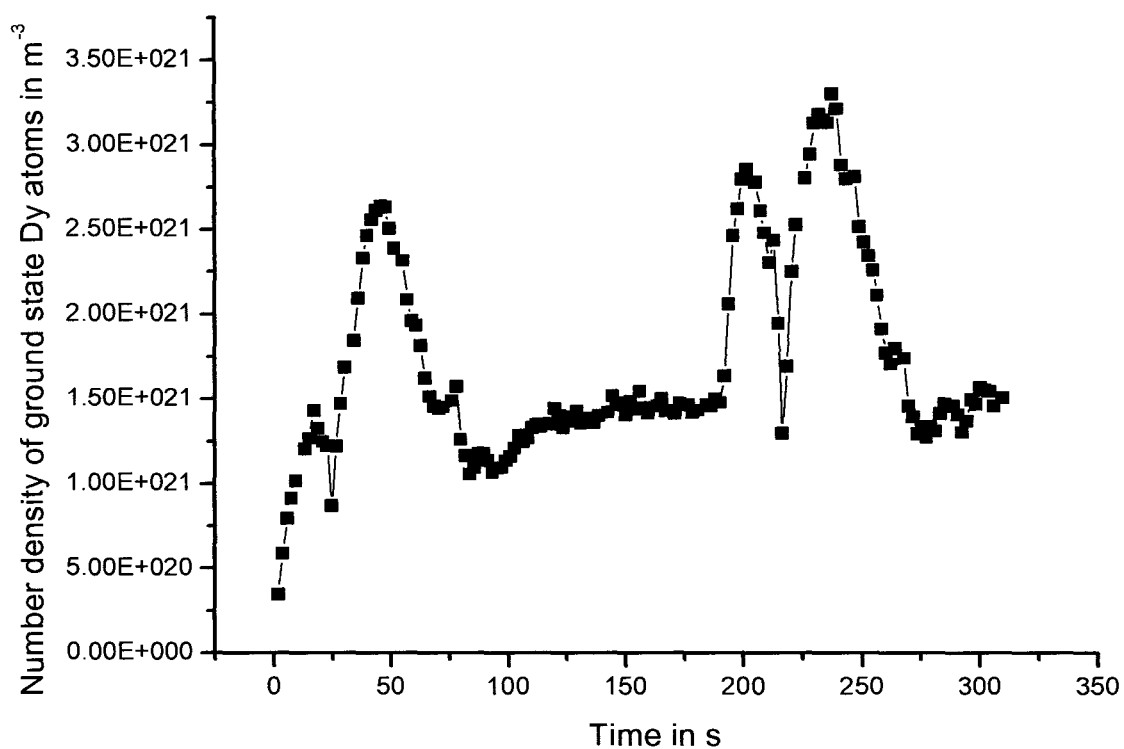The average number density within R^* versus time is pictured in Figure 28 and shows that during the first 1G phase for the 10mg Hg filled lamp, the number density is about $2.8*10^{21}m^{-3}$. Due to radial and axial segregation, the partial DyI_3 density is probably higher. How much higher is not known, if the variation is less than a factor of 3 Table 2 shows that this corresponds to a cold spot temperature of about 1090 to 1120K, which is the assumed temperature of the cold spot of 1100K [22]. The factor is assumed using Figure 10. The variations in atomic Dysprosium pressures differ not more than a factor of 3. We therefore conclude that with the absorption equation (3), a new and useful tool in examining plasmas is available.

For the rest of this chapter the effect of radial and axial segregation will be studied. Unfortunately, it is not possible to give a number density plot versus gravity. The 20s of 0G and 2G are not enough to end up in equilibrium in the burner of the lamp, because some processes in the lamp are too slow. Examples of these slow processes are the time constant discussed in the previous section and the diffusion of DyI_3 and Dy_2I_6. Note that this is the reason experiments were performed in the international space station ISS.

Normal 1G condition

The three lamps in Figure 28 probably have different cold spot temperatures, because they are all operated at 150W, but have different amounts of radiating particles in the discharge. Radiation is loss of energy so the temperature of the system (of which the cold spot is a part) will therefore be different.

Different mercury fillings result in different convective speeds in the lamp, more convection corresponds to less radial segregation and more radiating particles.

Different mercury fillings also mean different radial and axial segregation situations (Figure 6, Figure 8a and Figure 10). This in turn means that at equal cold spot temperature, different amounts of Dy atoms will be present in the discharge.

In order to compare the three lamps, the number density is normalized by dividing the number densities by the number density it had during 1G. The result of the normalization is shown in Figure 29.

First hyper G condition

Figure 29 shows that the number densities of all three lamps increase at the transition from 1G to 2G. This corresponds to less radial segregation (Figure 6) and a change from profile C to profile B in Figure 9, which means a decreasing axial segregation parameter and less axial segregation. Figure 8b shows that a decrease in axial segregation parameter with increasing G forces is possible, if the lamps are situated on the right hand side of the Fisher curve. On this side of the Fisher's curve, convection is dominant, which is in agreement with the diffusion and convection times estimated in Chapter 2 'Diffusion' and 'Convection'. The Dy atoms are carried further along the axis of the lamp by convection, before they pass the radius of molecular formation.

A slow decrease in density is also present in the 2G phase. This is due to a change in the energy balance of the lamp. There is more atomic Dysprosium in the plasma, so more energy is lost due to radiation. In addition, there is more convection, which is also a loss term. These two effects cause the cold spot temperature to decrease with equal input power (150W). The change in energy balance is essentially the same as the effect described in the section 'Startup phase of a lamp', i.e. establishing equilibrium in the burner. If the 2G situation would be longer, it could be possible that the density ends up lower than it was in 1G, regardless of radial segregation and their lower axial segregation parameters.

Zero G condition

At $t = 45s$ in Figure 29, the gravitational condition is changed from 2G to 0G. In zero G, radial segregation is maximal so fewer atoms are expected. In zero G $\lambda = 0m^{-1}$, corresponding to profile A in Figure 9. The atomic Dysprosium will spread along the axis of the lamp.

The density will drop, as pictured in Figure 29, because radial segregation is a relatively fast process. This is in agreement with the radial diffusion times of atomic Dysprosium ($\tau_{Dy\ diffusion} \approx 0.1s$).

The increase of atomic Dysprosium density due to the effect of axial segregation and is delayed, because the Dysprosium can only spread evenly over the discharge by means of diffusion along the axis of the lamp. The bigger Dysprosium related molecules situated just above the cold spot must supply the extra Dysprosium atoms. These molecules will diffuse more slowly. Once the molecules are in a high temperature zone, they will dissociate and more Dysprosium atoms will be detected.

In Table 5, estimations of diffusion times along the axis of the lamp are given. The table shows that for DyI_3 and Dy_2I_6, it will take 15 to 50s to travel along the axis of the lamp. For lower density lamps, the diffusion will be faster, which is in perfect agreement with Figure 29. The 5mg mercury filled lamp appears to be on the edge of reaching equilibrium at the end of the zero G phase.

The effect of the change in energy balance of the burner is also expected in this phase, but the segregation processes overshadows this effect.

Second hyper G condition

At $t = 70s$ in Figure 29, the gravitational condition changes from 0G to 2G. Convection will start again, so less radial segregation is expected and the lamp will travel the Fisher curve (Figure 8b) to the right hand side and end up at a higher axial segregation parameter, i.e. a lower density in the lamp and returning to profile B in Figure 9. Because convection times are about 0.1s, the change is faster compared to the transition from 2G to 0G. Further conclusions cannot be drawn from this phase, because the airplane in which the experiments are performed is not kept at a stable 2G during the second 2G phase.

At $t = 90s$ in Figure 29, the gravitational condition changes from 2G to 1G and the discharge will increase radial segregation and settle to profile C in Figure 9.
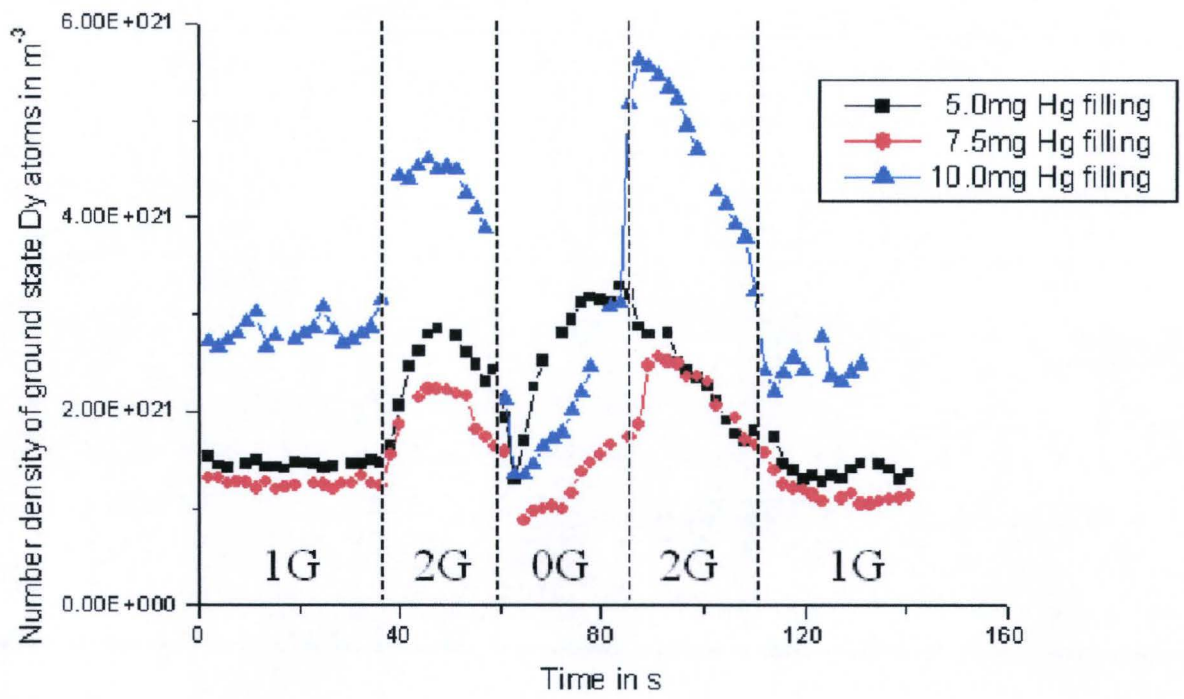
Figure 28: The number density measured in the three lamps during parabolas.
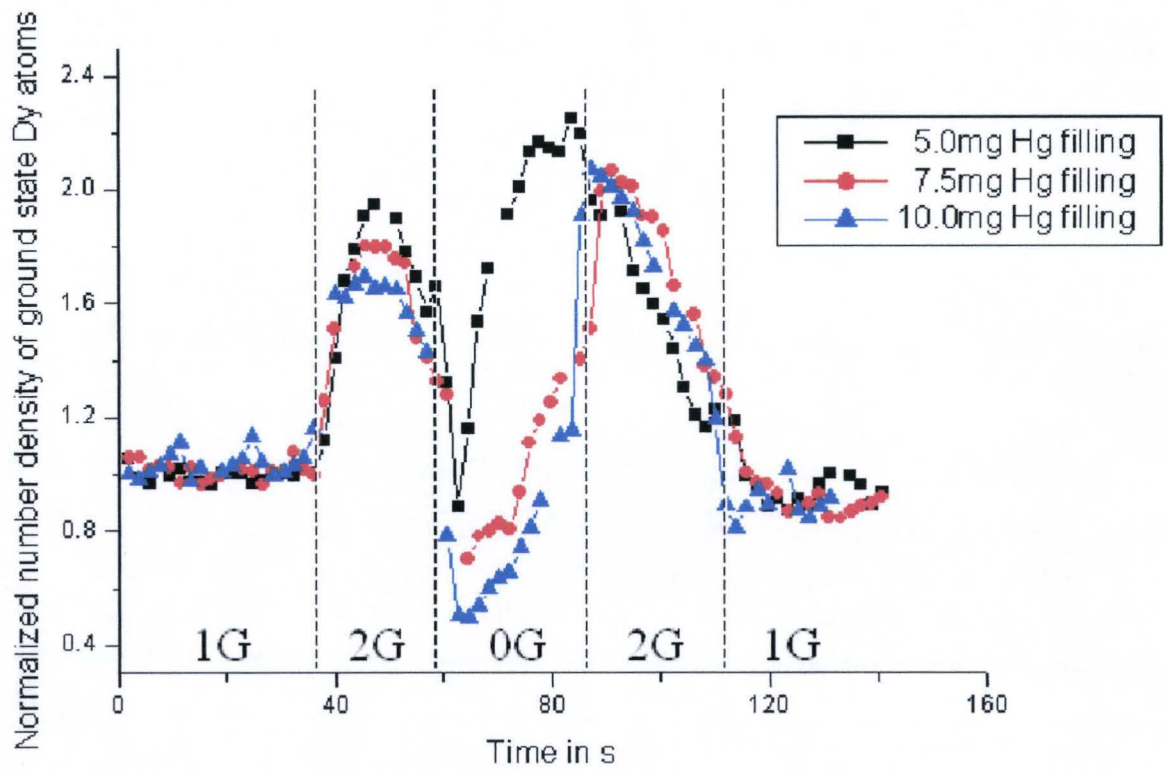
Figure 29: Normalized number density of ground state Dy atoms. The normalization is done by dividing the number density at each point by the number density in the 1G phase.

Chapter 5 Conclusions and recommendations

The following conclusions with respect to the measurement technique can be drawn from Chapter 2, Chapter 3 and Chapter 4:

- The absorption equation (3), derived by the author gives results that can be linked to literature values.
- Absorption spectroscopy is an accurate measurement technique by which ground state Dysprosium atoms can be detected.
- The data analysis technique, developed by the author, is robust. By integrating over the absorption line, it does not depend on the broadening of the absorption line.
- The technique CANNOT be used if stimulated emission appears or if spontaneous emission is not negligible compared to the intensity of the laser.

From the number density measurements presented in Chapter 3 and Chapter 4, we can conclude that:

- The settling of the energy balance of the burner of the lamp is a slow process. The time constant linked to this process is in the order of tens of seconds.
- We can see this effect at the startup of the lamps and at a gravitational transition, except for the transition from 2G to zero G. In zero G, slow diffusive effects overshadow this effect.
- The slope at the radius of molecular formation R^* is too steep for a third order polynomial to handle.
- The radius of molecular formation is about 3.2mm in burners with an inner radius of 4mm.
- Radial segregation, ionization and excitation reduces the number density of ground state Dysprosium atoms at the axis of the lamp.
- The number density of ground state Dysprosium atoms is maximal just before R^*.
- The three lamps are 'positioned' at the right hand side of the top of the Fisher curve, when gravity is 1G or 2G.
- In 0G, diffusion times of molecules determine the time it takes for the plasma to reach equilibrium and we saw that higher pressured lamps give longer diffusion times.
- The theory derived by Fisher can explain axial segregation.
- It is necessary to go to the ISS in order to examine HID lamps without convection and in equilibrium.

The author has the following recommendations:

- It could be of great interest to measure lamps with an Hg filling below 5mg and measure at the left hand side of the Fisher curve. ISS measurement are not needed for these experiments, because the 25s of zero G that can be obtained in PFC's should be enough to reach equilibrium.
- Computer simulations are needed to more accurately estimate diffusion and convection times.
- It may be possible to perform measurements without current coupling. This extends the scanning range from 0.2nm to 0.5nm, but introduces mode hops. The mode hops are in the order of 0.01nm, which could be small enough to be neglected. In order for this idea to be successful, the absorption and background measurements must be performed at the same time. The mode hops must appear at equal wavelengths in both measurements, because the signals must be divided in the data analysis.

Bibliography

[1]   Bax, M., *The design of a high resolution emission spectrometer for microgravity experiments on metal halide lamps*, Philips Trainee Report CDL 03/40009 or TU/e EPG 03-09 (2003).

[2]   Akker, D. v.d., *The design of a tunable diode laser absorption spectroscopy setup for measuring salt additives in metal-halide lamps in micro-gravity conditions*, Philips Trainee Report CDL 03/40010 (2003).

[3]   Schiffelers, G., *Study of gravity dependent radial de-mixing in metal halide lamps using spectroscopic techniques*, TU/e EPG 03-16 (2003).

[4]   Hout, F. van den, *Master Thesis (to be publised)*, Philips Trainee Report CDL (2004).

[5]   Kemps, P., *An experimental study of the radial additive density and plasma temperature profiles, and the effect of this on the integral light output of metal halide lamps as a function of gravity*, Philips Trainee Report CDL April (2004).

[6]   Stijfs, A., *Modeling segregation phenomena in metal halide lamps*, TU/e EPG 04-09 (2004).

[7]   Mullen, J.A.M. van der, *Excitation equilibria in plasmas; a classification*, Phys. Reports **191**, Numbers 2&3, July 1990.

[8]   Timmermans, E., *Atomic and molecular excitation processes in microwave induced plasmas*, PHD thesis, TU/e 1999.

[9]   Schram, D.C. and Engeln, R., *Inleiding plasmafysica*, TU/e PRO 218.

[10]   Thorne, A.P., *Spectrophysics*, Chapman and Hall & Science Paperbacks, London.

[11]   Fischer, E., *Axial segregation of additives in mercury-metal-halide arcs*, J. Appl. Phys. **47** 2954-2960 (1976).

[12]   Kurucz Atomic Line Database, http://cfa-www.harvard.edu/amdata/ampdata/kurucz23/sekur.html.

[13]   National Institute of Standards and Technology, *Physical Reference Database*, http://physics.nist.gov/PhysRefData/contents.html.

[14]   Software package Microcal Origin 6.0, http://www.OriginLab.com.

[15]   Haverlag, M., *Datasheets on partial Dysprosium pressures (not published)*, Philips CDL

[16]   Haverlag, M., *Datasheets on effective radii of particles in lamps (not published)*, Philips CDL

[17]   Sacher DLSpectroscopy V040907.pdf, http://www.sacher-laser.com.

[18]   Sacher, *Littman Laser user's manual: TEC 500*, October 14,2002.

[19]   http://www.webelements.com.

[20]   Vries, N. de, *Application of diagnostic techniques on high pressure mercury lamps*, TU/e EPG (2004).

[21]   Graaf, J. de, *Analyse 2*, page 57, TU/e (1998/1999).

[22]   Zhu, Xiao-Yan, *Ph.D. Thesis*, TU/e EPG (?).

[23]   Körber, A., *A simple delta lambda method for measurements of element pressures illustrated by application examples to HID lamps*, Aachen report PFL 1322/98 (1998).

[24]   Geijtenbeek, J.J.F., *The origin of demixing*, Philips Technical Note CDL 01/20125 (2001).

Appendices

Appendix A. Derivation of the absorption equation by Marc van Kemenade

The intensity change of a beam of radiation passing through plasma, i.e. both absorbing and emitting medium, can be represented by the differential equation [8]:

$$\frac{dI_\nu(s)}{ds} = -\kappa(\nu,s)I_\nu(s) + j_\nu(s)$$

(A.1)

with $I_\nu(s)$ the spectral intensity of the beam (in $Wm^{-2}sr^{-1}Hz^{-1}$), $j_\nu(s)$ the plasma emission coefficient (in $Wm^{-3}sr^{-1}Hz^{-1}$) and $\kappa(\nu,s)$ the absorption coefficient (in m^{-1}) for frequency ν (in s^{-1}) at location s (in m). In our case, the intensity from the laser is much higher than the emission by the plasma at the frequency in question. $j_\nu(s)$ is therefore neglected.

$$\frac{dI_\nu(s)}{I_\nu(s)} = -\kappa(\nu,s)ds$$

(A.2)

with

$$\kappa(\nu,s) = \frac{h\nu}{c}\left(B_{qp}n_q(s) - B_{pq}n_p(s)\right)\varphi_\nu(\nu,s)$$

(A.3)

In equation A.3 [8], the absorption coefficient is shown with h plank's constant, c the speed of light (in ms^{-1}), respectively B_{qp} and B_{pq} the Einstein coefficient for absorption and for stimulated emission, respectively n_q and n_p the number density of particles in state q and p (in m^{-3}) and $\varphi_\nu(\nu,s)$ the line shape of the optical transition at frequency ν (in s^{-1}). In Figure 30, a scheme with the three processes (i.e. spontaneous emission, absorption and stimulated emission) is shown between the two energy states.
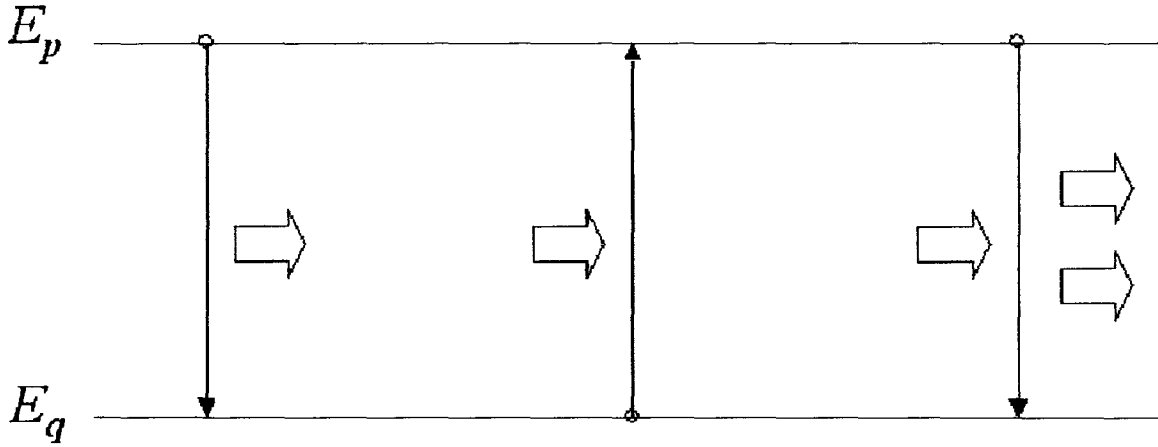
Figure 30: The three processes emission, absorption and stimulated emission between energy state p and q. With the slim arrow indicating the direction of the transition and the thick arrow the photons emitted or absorbed due to the transition.

For the line shape equation A.4 holds [8].

$$\int_0^\infty \varphi_v(v,s)dv \equiv 1 \tag{A.4}$$

Using the Einstein relations, i.e.

$$A_{pq} = \frac{g_q}{g_p} \frac{8\pi h v^3}{c^3} B_{qp} \tag{A.5}$$

$$g_q B_{qp} = g_p B_{pq} \tag{A.6}$$

with A_{pq} the coefficient for spontaneous emission and respectively g_q and g_p the allowed number of states in energy state q and p, equation A.3 yields

$$\kappa(v,s) = \frac{c^2}{8\pi v^2} \frac{g_p}{g_q} A_{pq} \left(n_q(s) - \frac{g_q}{g_p} n_p(s) \right) \varphi_v(v,s) \tag{A.7}$$

The allowed number of states in an energy state can be determined with [8]

$$g = 2J + 1 \tag{A.8}$$

In the next few lines, the explanation will be given to why the stimulated emission term from equation A.7 is neglected.

In our case, state p and q have equal quantum numbers J [13] and the number of states in these energy levels g_p and g_q are, therefore, also equal. If our lamps are in LTE, the Boltzmann distribution equation can be used

$$\frac{n_q}{g_q} = \frac{n_p}{g_p} \exp\left(-\frac{E_{pq}}{k_B T}\right)$$ (A.9)

which in our case becomes

$$n_q = n_p \exp\left(-\frac{E_{pq}}{k_B T}\right)$$ (A.10)

From equation A.10, we conclude that at $T\sim 0.5\text{eV}$, n_q will be about 2% of n_p.
Our lamps are in fact in non-TLE in which this percentage is even smaller. Stimulated emission can therefore be neglected from equation A.7. This yields

$$\kappa(v,s) = \frac{c^2}{8\pi v^2} \frac{g_p}{g_q} A_{pq} n_q(s) \varphi_v(v,s)$$ (A.11)

This equation can be simplified even further by taking into account that for the spectral line

$$\frac{\Delta\lambda_{pq}}{\lambda_{pq}} \ll 1$$ (A.12)

with $\Delta\lambda_{pq}$ the full width of the line and λ_{pq} the wavelength of the transition.
Equation A.11 can, therefore, be rewritten in

$$\kappa(v,s) = Sn_q(s)\varphi_v(v,s)$$ (A.13)

with

$$S = \frac{c^2}{8\pi v_{pq}^2} \frac{g_p}{g_q} A_{pq} = \frac{\lambda_{pq}^2}{8\pi} \frac{g_p}{g_q} A_{pq}$$ (A.14)

and $S = 2.65*10^{-9} \text{m}^2\text{s}^{-1}$ the line strength.
Combining equation A.2 and A.13 yields

$$\frac{dI_v(s)}{I_v(s)} = -Sn_q(s)\varphi_v(v,s)ds$$ (A.15)

or

$$\frac{d \ln I_v(s)}{ds} = -Sn_q(s)\varphi_v(v,s)$$ (A.16)

To get rid of the line shape function, equation A.16 is integrated over frequency, yielding

$$\int_0^\infty \frac{d \ln I_v(s)}{ds} dv = -Sn_q(s)$$ (A.17)

Consider the plasma and our measurement system, the plasma is assumed radically symmetric and measurements are done at points along the x-axis, which means the laser beam has traveled through the plasma along the y-axis. Figure 31 shows a schematic.
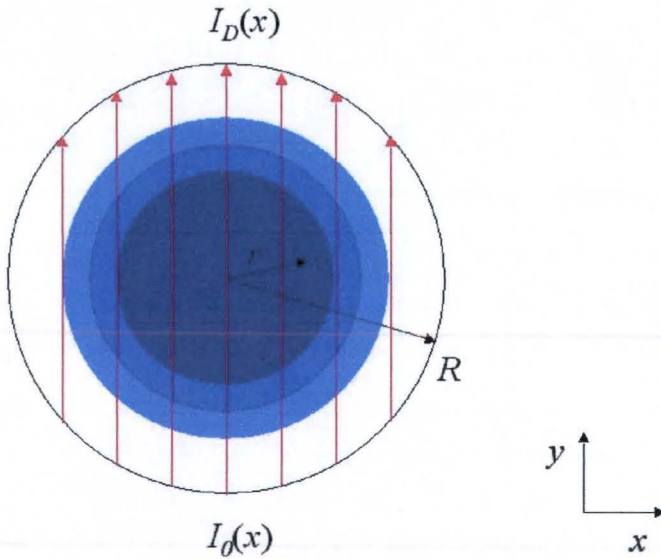

Figure 31: Schematic of the laser beam (red arrows) passing through the plasma in the burner with radius R.

Integrating equation A.16 over the line of sight gives

$$\int_{-\frac{1}{2}l(x)}^{\frac{1}{2}l(x)} \int_0^\infty \frac{d \ln I_v(y)}{dy} dv dy = -S \int_{-\frac{1}{2}l(x)}^{\frac{1}{2}l(x)} n_q(r) dy$$ (A.18)

With $l(x)$ the distance through the plasma.

50

$$\frac{1}{2}l(x) = \sqrt{R^2 - x^2}$$

(A.19)

If equation A.20 is a continuous function, the integration variables on the right hand side of equation A.18 are allowed to switch [21].

$$\frac{d \ln I_v(y)}{dy}$$

(A.20)

Equation A.20 is continuous, if the total absorption along the line of sight is not 100%.

$$\int_0^\infty \ln\left(\frac{I_{v,d}(x)}{I_{v,0}(x)}\right) dv = -2S \int_0^{\frac{1}{2}l(x)} n_q(r) dy$$

(A.21)

with $I_{v,0}$ the intensity before entering the plasma and $I_{v,d}$ the intensity on the detector, i.e. when the beam has passed through the plasma. Because our measurement system scans in wavelengths, equation A.21 is rewritten into

$$\int_0^\infty \ln\left(\frac{I_{\lambda,d}(x)}{I_{\lambda,0}(x)}\right) d\lambda = -\frac{\lambda_{pq}^4 A_{pq}}{4\pi c} \frac{g_p}{g_q} \int_0^{\frac{1}{2}l(x)} n_q(r) dy$$

(A.22)

To calculate the number density from the measurements, a basis of eigenfunctions is needed. One possibility is using $<1,r,r^2,r^3,...>$ from $r = 0$ to $r = R$, so:

$$n_q(r) = \sum_{n=0}^\infty a_n r^n \qquad \text{with } 0 \leq r < R$$

(A.23)

Equation A.22 becomes

$$\int_0^\infty \ln\left(\frac{I_{\lambda,d}(x)}{I_{\lambda,0}(x)}\right) d\lambda = -\frac{\lambda_{pq}^4 A_{pq}}{4\pi c} \frac{g_p}{g_q} \sum_{n=0}^\infty a_n f_n(x)$$

(A.24)

with $f_n(x)$ Abel polynomials of which the first five are listed in Appendix B. If the a_n's are known, so is the number density in the HID lamp.
Another possibility is not to use the inner radius of the burner R, but R^* which is defined as the radius at which all Dysprosium atoms disappear.

Appendix B. Some Abel polynomials

These are the first five Abel polynomials [2].

$$f_0(x) = \sqrt{R^2 - x^2}, \tag{B.1}$$

$$f_1(x) = \frac{1}{2}x^2 \ln\left(\frac{\sqrt{R^2 - x^2} + R}{|x|}\right) + \frac{1}{2}R\sqrt{R^2 - x^2}, \tag{B.2}$$

$$f_2(x) = x^2\sqrt{R^2 - x^2} + \frac{1}{3}(R^2 - x^2)^{3/2}, \tag{B.3}$$

$$f_3(x) = \frac{3}{8}x^4 \ln\left(\frac{\sqrt{R^2 - x^2} + R}{|x|}\right) + \frac{3}{8}Rx^2\sqrt{R^2 - x^2} + \frac{1}{4}R^3\sqrt{R^2 - x^2}, \tag{B.4}$$

$$f_4(x) = \frac{1}{5}(R^2 - x^2)^{5/2} + \frac{2}{3}x^2(R^2 - x^2)^{3/2} + x^4\sqrt{R^2 - x^2} \tag{B.5}$$

And

$$f_5(x) = \frac{5}{16}x^6 \ln\left(\frac{\sqrt{R^2 - x^2} + R}{|x|}\right) + \frac{5}{16}Rx^4\sqrt{R^2 - x^2} + \frac{5}{24}R^3x^2\sqrt{R^2 - x^2} + \frac{1}{6}R^5\sqrt{R^2 - x^2} \tag{B.6}$$

Appendix C. Origin script files

To calculate a density profile the following ORIGIN scripts [14], written by Marc van Kemenade, have to be executed:

- Script A on a background measurement,
- Script B on an absorption measurement,
- Script C, which is used by script B,
- Script D copies some windows,
- Script E copies some windows,
- Script F calculates the density profiles.

Script A

```
//Script A should be preformed on a window called RawBack and needs the templates Raw.OTW
//and Max.OTW. The rawBack window is an imported background measurement file like
//Pro_2004_0608_112804.Abs. The outputs of the script are two windows, which should be
//stored and used in script B/C. The windows are called Max$(mm) and ProfileLamp$(mm).


mm=15;
//mm is the number of the lamp

win -t data "C:\Documents and Settings\S465013.TUE\Mijn
documenten\Afstudeeropdracht\Origin functies\Raw.OTW" ResultFFT$(mm);
//this command creates a worksheet from the template Raw.OTW, which is stored in
// C:\Documents and Settings\S465013.TUE\Mijn documenten\Afstudeeropdracht\Origin functies

for(ii=1; ii<=33; ii++)
{ wks.col$(ii).name$ = AC$(ii-1); }
//this command renames the columns of the worksheet


%(ResultFFT$(mm),1) = %(RawBack$(mm),1);
//this command copies column 1 of worksheet RawBack$(mm) to ResultFFT$(mm)

curve.smoothpts = 25;
//this command sets FFT smoothing on 25 points before and after a point

for(ii=7; ii<=32; ii++)
{ curve.data$ = %(RawBack$(mm),$(ii+1));
  curve.result$ = %(ResultFFT$(mm),$(ii+1));
```

```
  curve.fftsmooth();
}
//here the measurements are FFT smoothened

win -t data "C:\Documents and Settings\S465013.TUE\Mijn
documenten\Afstudeeropdracht\Origin functies\Max.OTW" Max$(mm);
//this is part of the output of the script. It should be stored afterwards and used in script B.
//in this worksheet we store the maximal values of each scan

win -t data "C:\Documents and Settings\S465013.TUE\Mijn
documenten\Afstudeeropdracht\Origin functies\Raw.OTW" Shifted$(mm);
for(ii=1; ii<=33; ii++)
{ wks.col$(ii).name$ = BC$(ii-1); }


%(Shifted$(mm),1) = %(RawBack$(mm),1) - 654;
//row 654 has X=0
for(ii=7; ii<=32; ii++)
{ %(Max$(mm),1,ii) = ii;
  limit %(ResultFFT$(mm),ii+1);
  xx = limit.imax;
//maximum of scan is set on row 654
  %(Max$(mm),2,$(ii)) = xx;
  if (xx>654) { ss = xx-654;
          for(kk=1; kk<=1310-ss; kk++)
//from 1310-ss the cells are empty
          { %(Shifted$(mm),ii+1,kk) = %(RawBack$(mm),ii+1,kk+ss); }
          }
  if (xx<654) { ss = 654-xx;
          for(kk=1310; kk>=ss+1; kk--)
//before ss+1 the cells are empty
          { %(Shifted$(mm),ii+1,kk) = %(RawBack$(mm),ii+1,kk-ss); }
          }
  if (xx==654){ %(Shifted$(mm),ii+1) = %(RawBack$(mm),ii+1); }
}
//this part shifts the scans so the maxima are on X=0

win -t data "C:\Documents and Settings\S465013.TUE\Mijn
documenten\Afstudeeropdracht\Origin functies\Raw.OTW" ProfileLamp$(mm);
//this is part of the output of the script. It should be stored afterwards and used in script B.
//It stores the shifted and smoothened background measurement.

for(ii=1; ii<=33; ii++)
{ wks.col$(ii).name$ = Prof$(ii-1); }

%(ProfileLamp$(mm),1) = %(Shifted$(mm),1);
curve.smoothpts = 25;        //FFTsmoothing on 25 points before and after a point
```

```
for(ii=7; ii<=32; ii++)
{ curve.data$ = %(Shifted$(mm),$(ii+1));
  curve.result$ = %(ProfileLamp$(mm),$(ii+1));
  curve.fftsmooth();
}
```

Script B

```
//Script B should be preformed on windows called A1 to A12 and needs script C called
//MasterFile.ogs. The A windows are imported measurement files like
//Pro_2004_0608_112754.Abs. The outputs of the script are windows called Avalue1 to
//Avalue12.


freq=3*10^8/(642.19*10^(-9))^2;
towavelength=(1/655)*(40/100)*0.5*10^(-9);
//freq and to wavelength are to get a wavelength on the x axis
mm=18;
//mm is lampnumber
//nn is filenumber

for(nn=1; nn<=12; nn++){
run.section(C:\Documents and Settings\S465013.TUE\Mijn
documenten\Afstudeeropdracht\Origin functies\lab\bordeauxdata\MasterFile.ogs,SectionA);

run.section(C:\Documents and Settings\S465013.TUE\Mijn
documenten\Afstudeeropdracht\Origin functies\lab\bordeauxdata\MasterFile.ogs,SectionB);

run.section(C:\Documents and Settings\S465013.TUE\Mijn
documenten\Afstudeeropdracht\Origin functies\lab\bordeauxdata\MasterFile.ogs,SectionC);

run.section(C:\Documents and Settings\S465013.TUE\Mijn
documenten\Afstudeeropdracht\Origin functies\lab\bordeauxdata\MasterFile.ogs,SectionD);

run.section(C:\Documents and Settings\S465013.TUE\Mijn
documenten\Afstudeeropdracht\Origin functies\lab\bordeauxdata\MasterFile.ogs,SectionE);

run.section(C:\Documents and Settings\S465013.TUE\Mijn
documenten\Afstudeeropdracht\Origin functies\lab\bordeauxdata\MasterFile.ogs,SectionF);
//creates Dip

run.section(C:\Documents and Settings\S465013.TUE\Mijn
documenten\Afstudeeropdracht\Origin functies\lab\bordeauxdata\MasterFile.ogs,SectionG);
```

//creates AvDip

run.section(C:\Documents and Settings\S465013.TUE\Mijn
documenten\Afstudeeropdracht\Origin functies\lab\bordeauxdata\MasterFile.ogs,SectionI);
//creates Ln

run.section(C:\Documents and Settings\S465013.TUE\Mijn
documenten\Afstudeeropdracht\Origin functies\lab\bordeauxdata\MasterFile.ogs,SectionJ);
//creates Avalues with fitting
//run.section(C:\Documents and Settings\S465013.TUE\Mijn
documenten\Afstudeeropdracht\Origin functies\lab\bordeauxdata\MasterFile.ogs,SectionK);
//creates Avalues with integrating
//one must chose to run section J or section K

run.section(C:\Documents and Settings\S465013.TUE\Mijn
documenten\Afstudeeropdracht\Origin functies\lab\bordeauxdata\MasterFile.ogs,SectionL);
//deletes obsolete windows

}
//this section runs different parts of script C, stored as MasterFile.ogs in the folder C:\Documents
//and Settings\S465013.TUE\Mijn documenten\Afstudeeropdracht\Origin
//functies\lab\bordeauxdata.

Script C

//Script C is activated by script B and performs operations on windows called A1 to A12. The A
//windows are imported measurement files like Pro_2004_0608_112754.Abs. The script needs
//the templates Temps.OTW, Raw.OTW, HalfRaw.OTW, FourthRaw and Avalues.OTW and the
//output windows of script A Max$(mm) and ProfileLamp$(mm). The outputs of the script are
//windows called Avalue1 to Avalue12.

freq=3*10^8/(642.19*10^(-9))^2
towavelength= (1/655)*(40/100)*0.5*10^(-9);
mm=18;
//mm is lampnumber
nn=1;
//nn is filenumber

[SectionA]

```
//filenames starting with a T are Temporary
win -t data "C:\Documents and Settings\S465013.TUE\Mijn
documenten\Afstudeeropdracht\Origin functies\Temps.OTW" TA$(nn);
for(ii=1; ii<=33; ii++)
{ wks.col$(ii).name$ = F$(nn)A$(ii-1); }

for(jj=601; jj<=730; jj++)
{ %(TA$(nn),1,jj-600) = jj; }
for(ii=9; ii<=32; ii++)
{ for(jj=601; jj<=730; jj++)
  { %(TA$(nn),ii+1,jj-600) = %(A$(nn),ii+1,jj);
}}


[SectionB]

//filenames starting with a T are Temporary
win -t data "C:\Documents and Settings\S465013.TUE\Mijn
documenten\Afstudeeropdracht\Origin functies\Temps.OTW" TFFT$(nn);
for(ii=1; ii<=33; ii++)
{ wks.col$(ii).name$ = F$(nn)B$(ii-1); }

%(TFFT$(nn),1) = %(TA$(nn),1);
curve.smoothpts = 25;       //FFTsmoothing on 25 points before and after a point
curve.x$=%(TA$(nn),1);
for(ii=9; ii<=32; ii++)
{ curve.data$ = %(TA$(nn),ii+1);
  curve.result$ = %(TFFT$(nn),ii+1);
  curve.fftsmooth();
}


[SectionC]

//filenames starting with a S are Shifted
win -t data "C:\Documents and Settings\S465013.TUE\Mijn
documenten\Afstudeeropdracht\Origin functies\Raw.OTW" SA$(nn);
for(ii=1; ii<=33; ii++)
{ wks.col$(ii).name$ = F$(nn)C$(ii-1); }

%(SA$(nn),1) = %(ProfileLamp$(mm),1);    //row 654 has X=0
for(ii=9; ii<=32; ii++)                  //max of triangle is set on row 654
{ limit %(TFFT$(nn),ii+1);
  xx = limit.imax + 600;                 //in sectionA 600 was substracted
  %(Max$(mm),3,ii) = xx;
  if (xx>654) { ss = xx-654;
          for(kk=1; kk<=1310-ss; kk++)   //vanaf 1310-ss zijn cellen leeg
```

```
        { %(SA$(nn),ii+1,kk) = %(A$(nn),ii+1,kk+ss); }}
if (xx<654) { ss = 654-xx;
        for(kk=1310; kk>=ss+1; kk--)    //voor ss+1 zijn cellen leeg
        { %(SA$(nn),ii+1,kk) = %(A$(nn),ii+1,kk-ss); }}
if (xx==654){ %(SA$(nn),ii+1) = %(A$(nn),ii+1); }
if (xx<=601 || xx>700) {mark -m %(SA$(nn),ii+1) -b 1 -e 1310;}
}
```

[SectionD]

```
win -t data "C:\Documents and Settings\S465013.TUE\Mijn
documenten\Afstudeeropdracht\Origin functies\Raw.OTW" FFT$(nn);
for(ii=1; ii<=33; ii++)
{ wks.col$(ii).name$ = F$(nn)D$(ii-1); }

%(FFT$(nn),1) = %(SA$(nn),1); //this column will not be used
curve.smoothpts = 25;         //FFTsmoothing on 25 points before and after a point
for(ii=9; ii<=32; ii++)
{ curve.data$ = %(SA$(nn),ii+1);
  curve.result$ = %(FFT$(nn),ii+1);
  curve.fftsmooth();
}
```

[SectionE]

```
//filenames starting with a C are Corrected for background radiation
win -t data "C:\Documents and Settings\S465013.TUE\Mijn
documenten\Afstudeeropdracht\Origin functies\Raw.OTW" CFFT$(nn);
for(ii=1; ii<=33; ii++)
{ wks.col$(ii).name$ = F$(nn)E$(ii-1); }

%(CFFT$(nn),1) = %(FFT$(nn),1);  //this column will not be used
for(jj=9; jj<=32; jj++)
{ background = 0;
  for(ii=161; ii<=180; ii++)
  { background += %(FFT$(nn),jj+1,ii) - %(ProfileLamp$(mm),jj+1,ii); }
  for(ii=1131; ii<=1150; ii++)
  { background += %(FFT$(nn),jj+1,ii) - %(ProfileLamp$(mm),jj+1,ii); }
  background = background/40;
  for(ii=1; ii<=1310; ii++)
  { if (%(FFT$(nn),jj+1,ii)>0)  %(CFFT$(nn),jj+1,ii) = %(FFT$(nn),jj+1,ii) - background; }
}
```

[SectionF]

```
win -t data "C:\Documents and Settings\S465013.TUE\Mijn
documenten\Afstudeeropdracht\Origin functies\Raw.OTW" Dip$(nn);
for(ii=1; ii<=33; ii++)
{ wks.col$(ii).name$ = F$(nn)F$(ii-1); }


%(Dip$(nn),1) = %(CFFT$(nn),1);        //this column will not be used
for(jj=9; jj<=32; jj++)
{ for(ii=1; ii<=1310; ii++)
  { if (%(CFFT$(nn),jj+1,ii)>0 && %(ProfileLamp$(mm),jj+1,ii)>0) %(Dip$(nn),jj+1,ii) =
%(CFFT$(nn),jj+1,ii) / %(ProfileLamp$(mm),jj+1,ii); }
}


[SectionG]

win -t data "C:\Documents and Settings\S465013.TUE\Mijn
documenten\Afstudeeropdracht\Origin functies\HalfRaw.OTW" AvDip$(nn);
for(ii=1; ii<=33; ii++)
{ wks.col$(ii).name$ = F$(nn)H$(ii-1); }


for(ii=1; ii<=655; ii++)
{ %(AvDip$(nn),1,ii) = ii-1;}        //this column will not be used
for(jj=9; jj<=32; jj++)
{ for(ii=1; ii<=655; ii++)
  { %(AvDip$(nn),jj+1,ii) = ( %(Dip$(nn),jj+1,ii) + %(Dip$(nn),jj+1,1310-ii))/2;  }
}
mark -d %(AvDip$(nn),1) -b 631 -e 656;
mark -d %(AvDip$(nn),1) -b 1 -e 260;


[SectionI]

// - dip voor het fitten met een gauss A geeft de opp. onder de gauss
win -t data "C:\Documents and Settings\S465013.TUE\Mijn
documenten\Afstudeeropdracht\Origin functies\FourthRaw.OTW" Ln$(nn);
for(ii=1; ii<=33; ii++)
{ wks.col$(ii).name$ = F$(nn)J$(ii-1); }


for(ii=1; ii<=370; ii++){
%(Ln$(nn),1,ii) = ii;}


for(jj=9; jj<=32; jj++)
{ for(ii=1; ii<=370; ii++)
  { if(%(AvDip$(nn),jj+1,ii) > 0) { %(Ln$(nn),jj+1,ii) = - ln( %(AvDip$(nn),jj+1,ii) );  }
  }
}
```

[SectionJ]

win -t data "C:\Documents and Settings\S465013.TUE\Mijn
documenten\Afstudeeropdracht\Origin functies\Avalues.OTW" Avalue$(nn);

for(ii=1; ii<=2; ii++)
{ wks.col$(ii).name$ = F$(nn)K$(ii-1); }

nlsf.dataBegin=1;
nlsf.dataEnd=370;
nlsf.dataStep=1;
nlsf.func$="lorentz";
nlsf.x$=%(Ln$(nn),1);

for(ii=9; ii<=32; ii++){
  %(Avalue$(nn),1,ii)=ii;
  if(%(Ln$(nn),ii+1)!=){

    limit %(Ln$(nn),ii+1);
    itop = limit.imax;
    xtop = %(Ln$(nn),1,itop);
    nlsf.begin( );
    nlsf.y$=%(Ln$(nn),ii+1);
    nlsf.p1=0;
    nlsf.p2=xtop;
    nlsf.p3=120;
    nlsf.p4=20;

    nlsf.lb2=xtop-10;
    nlsf.ub2=xtop+10;

    nlsf.v1=0;
    nlsf.v2=1;
    nlsf.v3=1;
    nlsf.v4=1;

    nlsf.iterate(20);
    if(nlsf.nIter==20) { type "to few iterations"; }
    %(Avalue$(nn),2,ii)=nlsf.p4;
    nlsf.end( );
  }

60

```
}
%(Avalue$(nn),2) *= towavelength*freq;


nlsf.cleanUpFitData( );
nlsf.unInit( );

for(ii=1; ii<=32; ii++)
{ if( exist(NLSF$(ii))==2 )
  { NLSF$(ii)! Page.CloseBits=2;
    win -ca NLSF$(ii);
  }
}
```

[SectionK]

```
win -t data "C:\Documents and Settings\S465013.TUE\Mijn
documenten\Afstudeeropdracht\Origin functies\Avalues.OTW" Avalue$(nn);
for(ii=1; ii<=2; ii++)
{ wks.col$(ii).name$ = F$(nn)K$(ii-1); }


for(ii=9; ii<=32; ii++){
  %(Avalue$(nn),1,ii)=ii;
  if( %(Ln$(nn),ii+1)!= )
  { limit %(Ln$(nn),ii+1);
    top = limit.imax;
    %(Sum,1)=sum( %(Ln$(nn),ii+1) );
    %(Avalue$(nn),2,ii) = %(Sum,1,top) * 2;
  }
}

%(Avalue$(nn),2) *= towavelength*freq;
```

[SectionL]

```
window -c TA$(nn);
window -c TFFT$(nn);
window -c SA$(nn);
window -c FFT$(nn);
window -c CFFT$(nn);
window -c AvDip$(nn);
```

```
window -c Ln$(nn);
window -c Graph1;

window -a Dip$(nn);
window -i;
window -a Avalue$(nn);
window -i;
```

Script D

```
//This script copies the Avalue windows into one window called Aas$(ff).
//Aas$(ff) is a window with 13 rows and 33 columns.

ff=1;

%(Aas$(ff),1) = %(Avalue1,1);
wks.col$(1).name$ = Detnrf$(ff);
for(ii=1; ii<=12; ii++){

wks.col$(ii+1).name$ = Af$(ff)n$(ii);

%(Aas$(ff),ii+1) = %(Avalue$(ii),2);

}
```

Script E

```
//This script copies the Aas windows into one window called AllAas.
//The AllAas window has 32 rows and 86 columns.
//Column 2 has to be used to convert the detector number into postions in the lamp (in m).

wks.col$(1).name$ = Detnr;
wks.col$(2).name$ = LatPos;
%(AllAas,1) = %(Aas1,1);

for(jj=1; jj<=7; jj++) {
ff=jj;

for(ii=1; ii<=12; ii++){
```

```
wks.col$((ff-1)*12+ii+2).name$ = Avalue$((ff-1)*12+ii);

%(AllAas,(ff-1)*12+ii+2) = %(Aas$(ff),ii+1);


}

}
```

Script F

//This script gets the density profiles from the AllAas window and is put in the window Result.
//The script uses a user defined function called user1.
//The Result window has 84 rows and 5 columns.


```
S=2.65e-9;

nlsf.dataBegin=1;
nlsf.dataEnd=24;
nlsf.dataStep=1;
nlsf.func$="user1";
nlsf.x$=%(AllAas,2);

for(ii=1; ii<=84; ii++)
{ %(Result,1,ii) = ii;
  nlsf.begin( );
  nlsf.y$=%(AllAas,ii+2);
  nlsf.p1=0.00282;
  nlsf.p2=10^12;


  nlsf.v1=1;
  nlsf.v2=1;
  nlsf.iterate(20);
  if(nlsf.nIter==20) { type "to few iterations"; }
  %(Result,2,ii) = nlsf.p2/(2*S);
  %(Result,3,ii) = nlsf.e2/(2*S);
  %(Result,4,ii) = nlsf.p1;
  %(Result,5,ii) = nlsf.e1;
  nlsf.end( );
}
```

Appendix D. Occupation of the 20 carousel positions during the PFC

Table 8: Carousel filling during PFC of June 2004.

car. position	lampnr.	Hg (mg)	Additive	Burner diameter	
				"4mm"	"8mm"
1	F71	5,30	Ce	DGA	
2	-				
3	70	0,75	Dy	x	
4	73	2,00	Dy	x	
5	74	2,00	Dy	x	
6	-				
7	-				
8	-				
9	-				
10	-				
11	-				
12	-				
13	78	7,50	Dy		x
14	29	10,00	Dy		x
15	38	5,00	Dy		x
16	26	10,00	Ce		x
17	-				
18	79	7,50	Dy		x
19	30	10,00	Dy		x
20	41	5,00	Dy		x

Appendix E. The measurements performed during the PFC and used in this thesis

Table 9: Measurements used in thesis.

Lamp number	Mercury dose in HID Lamp in mg	Date of measurement	Starting time of measurements	End time of measurements	Time of background measurement
38	5	June 8 2004	11.38.01	11.43.52	11.43.54
79	7.5	June 9 2004	10.30.40	10.33.36	10.36.32
29	10	June 8 2004	10.45.34	10.48.32	11.48.33

Appendix F. Spectroscopic data of Dysprosium

Table 10: Spectroscopic data on Dysprosium [13].

Atomic number	66
Atomic mass	162.5u
Upper energy level of Absorption line	1.930239eV
J value of upper level	8
Lower energy level of Absorption line	0eV
J value of lower level	8
Transition wavelength λ_{pq}	642.19nm
Transition probability A_{pq}	$1.615*10^5 \text{s}^{-1}$
Oscillator strength f	$9.99*10^{-4}$
Ionization energy	6.82eV

Table 11: Partition sum of Dysprosium at different temperatures [12].

$T(\mathrm{K})$	$Q(T)$
2500	19.6
3000	21.1
3500	24.5
4000	27.9
4500	34.1
5000	40.3
5500	50.7
6000	61.0

Acknowledgements